

The Lack of Diffuse, Non-thermal Hard X-ray Emission in the Coma Cluster: The *Swift* BAT's Eye View

Daniel R. Wik¹, Craig L. Sarazin¹, Alexis Finoguenov^{2,3}, Wayne H. Baumgartner⁴, Richard F. Mushotzky⁵, Takashi Okajima⁴, Jack Tueller⁴, and Tracy E. Clarke⁶

ABSTRACT

The Coma cluster of galaxies hosts the brightest radio halo known and has therefore been the target of numerous searches for associated inverse Compton (IC) emission, particularly at hard X-ray energies where the IC signal must eventually dominate over thermal emission. The most recent search with the *Suzaku* Hard X-ray Detector (HXD) (Wik et al. 2009) failed to confirm previous IC detections (Rephaeli & Gruber 2002; Fusco-Femiano et al. 2004), instead setting an upper limit 2.5 times below their nonthermal flux. However, due to the relatively smaller field of view of the HXD, this discrepancy can be resolved if the IC emission is very extended, beyond the scale of the cluster radio halo. Using reconstructed sky images from the 58-month *Swift* BAT all sky survey, the feasibility of such a solution is investigated. Building on Renaud et al. (2006), we test and implement a method for extracting the fluxes of extended sources, assuming specified spatial distributions. Thermal and nonthermal spatial distributions appropriate for the Coma cluster are simultaneously fit to the 8 energy bands that make up the BAT survey data; the spatial distribution of the detected emission is found to be consistent with a purely thermal origin. The resulting spectra are then jointly fit with an *XMM-Newton* EPIC-pn spectrum derived from mosaic observations. We find no evidence for large-scale IC emission at a level sufficient to reconcile the *Suzaku* upper limit with the previous detections. For all nonthermal spatial distributions considered, which span the gamut of physically

¹Department of Astronomy, University of Virginia, P. O. Box 400325 Charlottesville, VA 22904-4325; drw2x@virginia.edu

²Max Planck Institute for Extraterrestrial Physics

³Center for Space Science Technology, University of Maryland Baltimore County

⁴Laboratory for High Energy Astrophysics, NASA Goddard Space Flight Center

⁵Department of Astronomy, University of Maryland, College Park

⁶Naval Research Laboratory

reasonable IC models, we determine upper limits for which the largest (most conservative) limit is $\lesssim 4.2 \times 10^{-12} \text{ erg s}^{-1} \text{ cm}^{-2}$ (20–80 keV), which corresponds to a lower limit on the magnetic field $B > 0.2 \mu\text{G}$. A nominal flux upper limit of $< 2.7 \times 10^{-12} \text{ erg s}^{-1} \text{ cm}^{-2}$, with corresponding $B > 0.25 \mu\text{G}$, is derived for the most probable IC distribution given the size of the radio halo and likely magnetic field radial profile.

Subject headings: galaxies: clusters: general — galaxies: clusters: individual (Coma) — intergalactic medium — magnetic fields — radiation mechanisms: non-thermal — X-rays: galaxies: clusters

1. Introduction

The X-ray emission from clusters of galaxies is primarily thermal in origin and is produced by a diffuse population of intergalactic electrons in the ionized intracluster medium (ICM). These electrons coexist with a nonthermal, relativistic electron population in at least some clusters – inferred from observations in the radio regime – which should also radiate at X-ray energies. While thermal emission clearly dominates in the kilo-electron volt (keV) energy range, it declines rapidly outside this range, allowing the detection of a nonthermal spectral signature as soft or hard excess emission. This possibility is especially promising at hard (>10 keV) energies, where the exponential decline of the thermal bremsstrahlung continuum is distinctly steeper than the expected nonthermal spectrum. Measurements of nonthermal X-ray emission are critical to the determination of the total amount of relativistic constituents in the ICM, which is currently poorly constrained. While no more than $\sim 10\%$ of the energy in the ICM is tied up in nonthermal components, amounts at or near this level will affect the dynamics and structure of the thermal gas (e.g., Vazza et al. 2009). Specifically, studies that attempt to infer the total masses of clusters from the hydrostatic state of the thermal gas will produce biased mass estimates if the pressure support of relativistic particles and fields is not accurately included. Such mass estimates are the cornerstone from which cluster mass functions are built, which can be used to constrain cosmological parameters; these studies are already underway using observables derived in both the X-ray (e.g., Mantz et al. 2008; Vikhlinin et al. 2009) and microwave (e.g., Vanderlinde et al. 2010, through the Sunyaev-Zel’dovich effect) regimes.

A measurement of the total energy in relativistic ICM components is possible when X-ray and radio nonthermal fluxes are combined. Diffuse, cluster-wide synchrotron radio emission, called radio halos or relics depending on their morphology, imply that both magnetic fields and relativistic electron populations are present on large scales. The total luminosity of a

synchrotron-emitting electron is given by

$$L_R = \frac{4}{3}\sigma_T c \gamma^2 \epsilon_B, \quad (1)$$

where σ_T is the Thomson cross-section, c is the speed of light, γ is the Lorentz factor of the electron, and $\epsilon_B = B^2/8\pi$ is the energy density of the magnetic field. For a collection of relativistic electrons, the value of L_R depends both on the number of electrons and on B and cannot independently determine either. However, these same electrons will up-scatter cosmic microwave background (CMB) photons through inverse Compton (IC) interactions, which have a luminosity L_X equivalent in form to equation (1) but with ϵ_B replaced by the energy density of the CMB. Since both luminosities are proportional to the number of electrons, their ratio gives the volume-averaged magnetic field,

$$\frac{L_R}{L_X} = \frac{B^2/8\pi}{aT_{CMB}^4}, \quad (2)$$

where a is the radiation constant and T_{CMB} is the temperature of the CMB. The IC radiation should be observable at hard X-ray energies (Rephaeli 1977). Thus far, IC emission has only been detected at low significance (Nevalainen et al. 2004; Million & Allen 2009) or, in one case, in a cluster with uncertain radio emission (Eckert et al. 2008; but see also Ajello et al. 2009 and Fujita et al. 2008). The measurement of an IC flux from a synchrotron source directly leads to a simultaneous determination of the average value of B and the relativistic electron density (Harris & Romanishin 1974; Sarazin 1988). Therefore searches for IC emission coincident with a radio halo or relic are an excellent way to constrain the contribution of relativistic materials in clusters.

The first, and brightest, radio halo was discovered by Willson (1970) in the Coma cluster, and its radio properties have perhaps been the best studied (e.g. Giovannini et al. 1993; Deiss et al. 1997; Thierbach et al. 2003). Coma has been observed by all the major observatories with hard X-ray capabilities (Henriksen & Mushotzky 1986; Bazzano et al. 1990; Hughes et al. 1993; Rephaeli et al. 1994), and more recently non-thermal detections have been claimed by Rephaeli & Gruber (2002) with *RXTE* and by Fusco-Femiano et al. (1999, 2004) with *BeppoSAX*, though the latter detection is controversial (Rossetti & Molendi 2004; Fusco-Femiano et al. 2007). Due to the large field of view (FOV) of these non-imaging instruments and the simple characterization of the thermal gas, the source of this emission remains uncertain. Even more recently, long (~ 1 Msec) observations with *INTEGRAL* have imaged extended diffuse hard X-ray emission from Coma, though it was found to be completely consistent with thermal emission (Renaud et al. 2006; Eckert et al. 2007; Lutovinov et al. 2008).

Most recently, Wik et al. (2009) performed a joint analysis of spectra from the *XMM-Newton* EPIC-pn and *Suzaku* HXD-PIN instruments – the most sensitive instruments at soft

and hard energies to date – of the Coma cluster and were unable to detect IC emission. Instead, they found an upper limit 2.5 times below the detections of Rephaeli & Gruber (2002) and Fusco-Femiano et al. (2004). However, the narrower FOV of the HXD relative to the collimators of the *RXTE* PCA/HEXTE and *Beppo-SAX* PDS leaves open the possibility that the spatial distribution of IC photons is highly extended, and therefore much of the flux was missed by the HXD. The IC would have to be much broader than the size of the radio halo. A uniform IC surface brightness of at least $30'$ in radius from the cluster center is sufficient to reconcile these results. Therefore, an imaging analysis at hard X-rays is required to confirm this picture; unfortunately, no focussing hard (>10 keV) X-ray telescope has yet been deployed. In the meantime, it is possible to perform a crude imaging analysis with coded mask instruments, as previously discussed by Renaud et al. (2006).

In this work, we report on the spatial and spectral hard X-ray emission from the Coma cluster using the 58-month accumulation of the *Swift* Burst Alert Telescope (BAT) all-sky survey. From the first 9 months of the survey, Coma is clearly extended (Ajello et al. 2009), and so an accurate measurement of its flux must account for this fact. Using models for the spatial distribution of thermal and potential nonthermal emission, we measure the total, extended flux in the 8 energy bands that make up the survey. These fluxes are then converted into spectra, which we jointly fit with an *XMM-Newton* EPIC-pn spectrum from a *spatially identical region*. In this way, despite poor spatial resolution ($\sim 20'$), we are sensitive to any large-scale, extended emission above the detection threshold for the survey. While the sensitivity of the BAT detector is lower than instruments such as the *Suzaku* HXD-PIN, the survey’s large exposure time – thanks to a FOV that sees $1/8^{\text{th}}$ of the sky in a single pointing – gives it a comparable, if not superior, overall sensitivity. In Section 2, we describe the *Swift* BAT survey in general and the *XMM-Newton* EPIC-pn and BAT observations of the Coma cluster specifically. The extraction of spatially extended fluxes from models, along with the specific models themselves, is discussed in Section 3. Spectra constructed from these spatial fits are presented in Section 4, along with the results of joint fits with the *XMM-Newton* spectrum. In Section 5, we provide upper limits on spatially extended, nonthermal emission, and in Section 6 we discuss the implications of our non-detection for the relativistic phase of the ICM of the Coma cluster. In the appendices, we describe the calibration of the survey such that joint fits with *XMM-Newton* are straightforward, and we demonstrate that the BAT instrument intrinsically detects extended emission on the scales of interest here, though with higher uncertainty than for a point source. We assume a flat cosmology with $\Omega_M = 0.23$ and $H_0 = 72$ km/s/Mpc and a luminosity distance to Coma of 98.4 Mpc. Unless otherwise stated, all uncertainties are given at the 90% confidence level.

2. Observations

To achieve the necessary spatial coverage and spectral sensitivity, we take advantage of mosaics of the Coma cluster constructed from observations by the *XMM-Newton* and *Swift* satellites. The high sensitivity and good spectral and spatial resolution of the *XMM-Newton* EPIC-pn data act as a check on the interpretation of the *Swift* BAT data, allowing the thermal and potentially nonthermal emission at hard energies to be accurately decoupled.

2.1. *XMM-Newton* EPIC-pn Mosaic Observations

The observations and processed *XMM-Newton* data used herein are identical to that presented in Wik et al. (2009), where a more detailed description can be found. The *XMM-Newton* EPIC-pn mosaic of Coma consists of 14 individual pointings, the first set (11 pointings) of which were discussed in Briel et al. (2001). The full 14 pointings considered here were first presented in Schuecker et al. (2004). For joint fitting with *Swift* BAT spectra, we extract events from a $65'.5 \times 65'.5$ box centered on the radio halo, which was originally chosen to match the *Suzaku* Hard X-ray Detector field of view; the region is shown as the outermost contour in Figure 3 of Wik et al. (2009), and also as the box in Figure 1 in the present paper. The only modification of our analysis procedure compared to that in Wik et al. (2009) is that the *XMM-Newton* spectra were not weighted by the spatial response of the *Suzaku* HXD, since they are not being fit simultaneously with that instrument. No similar weighting is needed to comparison to the *Swift* BAT data since the BAT survey covers the entire sky and the vignetting of individual pointings is corrected for during processing.

We also use the temperature map derived from the *XMM-Newton* mosaic and described in Wik et al. (2009) to model the spatial distribution of hard X-ray emission, which is detailed in Section 3.1.1. Spectra extracted within a 16×16 contiguous grid of regions of size $4'.3 \times 4'.3$ are fit to single temperature APEC models over the energy range $0.5 < E < 14$ keV.

While data from the *Suzaku* observation of Coma (OBSID 801097010) are not part of the current analysis, we do make use of the 2–7.5 keV spectrum from the 0 chip of the X-ray Imaging Spectrometer (XIS0) for calibration purposes, as described in Section A.1. We use the same spectrum that served to cross-calibrate the data in the previous *XMM-Newton/Suzaku* analysis (region 10 from Wik et al. 2009).

2.2. The *Swift* BAT 58–Month Survey

The *Swift* mission is primarily to detect and localize gamma-ray bursts, which is accomplished with the very large FOV ($\sim 1/8^{\text{th}}$ of the sky), coded mask aperture Burst Alert Telescope (BAT). As such, the nearly random pointing strategy culminates in an almost uniform coverage of the entire sky with an ~ 8 Ms of exposure time, made from many ~ 5 minute individual observations. Images of the sky are reconstructed by cross-correlating the shadow pattern of the randomly coded mask in front of the detectors with the detector pixels via a fast Fourier transform. The detectors are sensitive to hard X-ray/soft gamma-ray photons from 14–195 keV in 80 native energy channels. As part of the default survey processing, the channels are combined into 8 broader energy bands: 14–20 keV (E1), 20–24 keV (E2), 24–35 keV (E3), 35–50 keV (E4), 50–75 keV (E5), 75–100 keV (E6), 100–150 keV (E7), and 150–195 keV (E8). The final survey is built from the individual sky reconstructions, which are summed and resampled onto predetermined image planes of 6 facets, each in the Zenith Equal Area projection. The detailed processing methodology and survey properties for the 58-month BAT all sky survey are nearly identical to those described in Tueller et al. (2010) for the 22-month survey. The only major difference is that for the 58-month survey, the gain of each detector pixel was *individually* calibrated with an onboard radioactive source, which had not been done previously. This better accounts for the sensitivity of low gain pixels, effectively increasing the overall sensitivity. Also, the sky images are more finely resampled so that the pixels near the center of the image projection scale $2'8$ instead of $5'$ as with previous versions of the survey. The main advantage of this change is to improve the centroiding of sources.

Because the systematic uncertainties in the survey-averaged spectrum of the Crab Nebula are smaller than the uncertainties in the BAT survey response matrix, BAT survey fluxes are tied to the Crab fluxes in each band (see Tueller et al. 2010, Sec. 4.5). One drawback to this approach is that a source flux is only guaranteed to be correctly determined if its spectrum within the energy band is identical to the Crab’s (a power-law with a photon index of $\Gamma \sim 2.1$), since the energy response within the band may not be uniform. Because we will fit the BAT spectrum jointly with the *XMM-Newton* spectrum, it is important that the cross-calibration between the *Swift* BAT and *XMM-Newton* be accurate. Since the flux calibration of the BAT survey is based on the Crab spectrum, we have made sure that the *Swift* BAT and *XMM-Newton* agree on the flux and spectrum of the Crab. The cross-calibration between *Swift* BAT and *XMM-Newton* is discussed in detail in Appendix A.

2.2.1. The Coma Cluster

The 6 facets are oriented in Galactic coordinates with one facet centered on each of the Galactic poles and the other 4 centered uniformly around the Galactic plane. The Zenith Equal Area projection conserves surface brightness but not shapes, so objects far from the center of the projection can be somewhat distorted. However, the fortuitous location of the Coma cluster near the North Galactic pole, and thus the center of its facet, means that any such distortions are negligible. Nevertheless, for all parts of the analysis image pixels are referred to in terms of their Galactic coordinates so that any image projection effects are completely eliminated.

Hard X-ray emission is clearly detected in the first 4 energy bands, up to 50 keV. In Figure 1, we present the wavelet-smoothed 2–7 keV *XMM-Newton* EPIC-pn image of the Coma cluster mosaic overlaid with contours of the Crab-weighted BAT flux (see Tueller et al. 2010, for a description), which shows the hard X-ray emission to be elongated in the same East-West direction as the softer emission. As first noted by Ajello et al. (2009) in the 9-month BAT survey, the Coma cluster is partially resolved by the BAT, which is explicitly shown in Figure 2. This figure compares the radial surface brightness profile of Coma with that of a nearby point source with a comparable flux. Coma is clearly extended. The points plotted are individual pixels. The greater width of the distribution for Coma indicates that its surface brightness is not circularly symmetric. As shown in Figure 1, both the BAT and *XMM-Newton* X-ray emission is elongated in a ENE-WSW direction.

While coded masks instruments have some difficulty detecting extended emission, this is only true for emission extended on very large scales, when the shadow pattern of the mask on the detector plane becomes sufficiently blurred; for the BAT, simulations suggest that this scale, *in principle*, approaches the size of the FOV. The actual problem is that flux from each part of an extended source adds systematic noise to every other part of the source, eventually drowning the signal in a sea of noise. However, for small extensions this additional uncertainty is not overwhelming, especially if the rough flux distribution is already known. In Appendix B, we show that the *Swift* BAT provides accurate fluxes for extended sources on the scale of interest for the Coma cluster.

Because nearby pixels in the BAT survey images are correlated, it is more difficult to determine the flux uncertainties for extended sources in the BAT than is usually the case for X-ray images. For point sources, the flux uncertainties can be determined from the fluctuations in the local background in the BAT survey images. For Coma, we calculate the RMS fluctuations in the background (σ_{bgd}) around Coma in an annulus of radius $15 < r < 100$ pixels ($42' < r < 4^\circ.67$), as is typically done for sources in the BAT survey. These values, and the flux uncertainties for extended sources like Coma, are derived in Appendix C.

3. Characterization of Extended Emission in BAT Images

To extract fluxes for extended sources, we choose to test *a priori* model distributions, as opposed to using a method like the “CLEAN” algorithm (Högbom 1974), which reconstructs fluxes from an unknown underlying distribution assuming the PSF shape only. (See Appendix B.2 for details about this choice.) We represent a diffuse source as a collection of point sources, each of which is convolved by the PSF (Eqn. B1) and summed together. Throughout this work, image data are fit to these spatial models using the MPFIT algorithm (Markwardt 2009), which performs a Levenberg-Marquardt least-squares minimization to converge on best-fit parameter values.

3.1. Model Spatial Distributions of Hard X-ray Emission

Our goal is to detect IC emission from the same electrons producing the radio halo; however, the electron spatial distribution need not follow the radio halo if B varies spatially within the ICM. Indeed, there is evidence that the magnetic field in Coma declines with radius (Bonafede et al. 2010), which would allow for a more extended relativistic electron population visible through IC interactions with CMB photons. To accurately search for this potential signal, we need to both choose model distributions for this emission and to fully model the thermal emission also present in the BAT energy bands.

3.1.1. Thermal Models

Following the success of the *XMM-Newton*-derived temperature map for explaining the thermal origin of the *Suzaku* HXD-PIN spectrum (Wik et al. 2009), we use the same map to predict the spatial distribution of thermal emission at hard energies. For each region of the map, the flux of the best-fit APEC model is calculated in each BAT energy band and treated as a point source at that location. Note that because the APEC and MeKaL models are not defined above 50 keV in XSpec, we use MeKa to derive the temperature map fluxes in the 4 highest energy bands. Then, for each band the 232 temperature map region “points” are taken together to serve as the diffuse model. To compare this or any of our diffuse models to the BAT image data, each point is assigned the PSF shape with its peak value equal to the point flux, and the overlapping PSFs are summed together and sampled at the location of the image pixels.

Thermal emission is detected in the first 4 BAT energy bands E1–E4. Since this emission is an extension of the X-ray emission which dominates the *XMM-Newton* image and its

distribution is known, we fix the location of the thermal model to the best-fit position of the model for the E1 band data, where the signal-to-noise ratio is the highest.

Note that for the thermal model “fits” to the *Swift* BAT spatial distribution in various bands, only the normalization of the model in each band is allowed to vary. The spatial distribution within each of the bands is completely determined from the *XMM-Newton* data.

The *XMM-Newton* data will also contain any nonthermal emission within the *XMM-Newton* band. Is it reasonable to use the *XMM-Newton* temperature map and image to determine the spatial distribution of the hard X-ray thermal emission? The spectra in the temperature map were fit over the energy range $0.5 \text{ keV} < E < 14 \text{ keV}$. While the upper limit of this band is fairly hard, the low energy limit guarantees that the spectra are dominated by softer photons. For any sensible nonthermal spectrum, the *XMM-Newton* spectra are dominated by thermal emission. In fact, if there is cool, dense gas along a given line of sight, the *XMM-Newton*-based model may actually underestimate the thermal hard X-ray emission. In any case, if there is strong nonthermal emission in the *XMM-Newton* spectrum, it will dominate the harder BAT energy bands, and will be uncovered in the joint spectral fits to the *XMM-Newton* and BAT spectra (Section 4 below).

3.1.2. Nonthermal Spatial Models

The *Suzaku* HXD-PIN upper limit, which is 2.5 times below the *RXTE* and *Beppo-SAX* detections, only excludes those measurements if the IC emission originates from a relatively compact region ($R \lesssim 20'$). More extended emission of roughly uniform surface brightness, however, would be consistent with both the detections and upper limit. In most physical models for the IC, it is likely that the surface brightness would decline with radius; one exception is the KW model discussed below. However, there is no single well-established model for this decline. Since our object is to test the possibility that the difference between our *Suzaku* HXD-PIN upper limit and the *RXTE* and *Beppo-SAX* detections is due to the extent of the IC emission, we consider the extreme case of a uniform surface brightness disk. Thus, we assume any nonthermal emission to take the form of a uniform brightness, circular disk with a radius $R = 25'$ (R25), $30'$ (R30), $35'$ (R35), $40'$ (R40), $45'$ (R45), or $60'$ (R60).

Recently, Kushnir & Waxman (2010) proposed another model for the IC emission of the Coma cluster which is consistent with both the *Suzaku* HXD-PIN upper limit and the *RXTE* and *Beppo-SAX* detections. In this model, the IC hard X-ray emission comes from a separate population of electrons from those in the radio halo. This new population of electrons are accelerated at the virial accretion shock of the cluster at a very large radius.

These virial shock accelerated electrons lose energy quickly, and form a shell of hard X-ray emission, which projects on the sky as a ring with nearly uniform surface brightness emission in its interior. We will refer to this as the KW model. While most of the flux resides in a ring at the cluster virial radius, the amount of flux detected by an instrument pointed at the cluster center will depend sensitively on its FOV. We take all the model parameter values for Coma directly from Kushnir & Waxman (2010) when comparing their expected flux to the constraints imposed by the BAT data, though the only relevant parameter for the spatial distribution is the accretion shock radius $\theta_{200} = 82''.1$. The radial distribution of flux is simply geometrical in form, assuming an infinitely thin shell at this radius; the expression is given in Kushnir & Waxman (2010, Eqn. 9).

In reality, it is unlikely the spatial distribution of emission would be as regular and axisymmetric as portrayed by these models. However, for the spatial extent we consider relative to the resolution of the BAT, deviations from the idealized models will not particularly impact our results.

We do not assume that the center of the nonthermal emission distribution from Coma is the same as the center of the thermal emission. Instead, for each of the nonthermal models, the model center is placed at 81 different positions on a 9×9 grid with $2''.5$ spacings around the centroid of the large-scale thermal emission. The center of the nonthermal emission is taken as one of the parameters to be varied in the fits of the spatial and spectral distributions below.

3.2. Spatial Fits to the BAT data

The spatial models for the thermal emission alone, or for the thermal emission plus nonthermal emission, were fit to the pixel values in the BAT images in each of the 8 BAT bands. As noted above (Section 3.1.1), the center of the thermal model was determined by fitting the center in the E1 band. For the thermal model, only the overall normalization was allowed to vary. For the nonthermal models, the center was varied for a grid of positions (but fixed in each individual fit, see Section 3.1.2). The model normalization (i.e., flux) in each of the 8 BAT bands was fit independently for the thermal and nonthermal models. That is, the spatial fits made no assumptions about the spectrum of either type of emission.

In Figure 3, we present the *Swift* BAT images of Coma in all 8 energy bands (first and third columns) along with the thermal model-subtracted residuals for bands E1–E4 (center column). The spatial distribution of the thermal models is represented with the contours in the first column. Note that only positively-valued pixels appear in the grayscale, which has

a square-root scaling, and that for each band pure black corresponds to a slightly different value. Each panel covers an identical 2.7×1.5 region of the sky. Residuals from the fits are consistent with background fluctuations, as can also be seen in the radial profiles shown in Figure 4.

As noted above (Section 3.1.1), these thermal models are solely based on the *XMM-Newton* temperature map. That is, the spatial distribution is completely determined from the *XMM-Newton* data, and only the normalization is allowed to vary. Still, this thermal model provides an adequate description of both the spatial and spectral (discussed in Section 4 below) properties of the detected emission in the BAT data. This success justifies our approach and confirms that extended emission is detected with the same efficiency as that from the cluster center.

The good fit of the *XMM-Newton*-based thermal model for the emission in BAT bands E1–E4 and the lack of obvious excess emission in the harder E5–E8 bands suggests that nonthermal emission is not very strong or extended. The nonthermal model with the most extended emission is the KW model (Kushnir & Waxman 2010), in which the IC hard X-ray emission comes from a thin shell at a very large radius. Following the methodology in Section B.2, we simulate the expected combined thermal and nonthermal flux distribution for this model, and compare to the actual data. The results for the E1 BAT band are shown in the upper panel of Figure 5. Clearly, we do not detect the nonthermal emission expected by the KW model. The lower panel shows the thermal plus KW model compared to a simulation of the BAT data assuming the distribution actually followed this model. It is clear that the statistics in the BAT data would allow us to detect the nonthermal emission from the KW model, were it present. A more quantitative limit is derived in Section 5.

4. Spectral Fits

To search for a nonthermal component in the X-ray spectrum of the Coma cluster, spectral models are fit to the data. The fits were done for the *Swift* BAT spectrum alone, or simultaneously with the *XMM-Newton* spectrum of the cluster. The BAT spectra were binned into 8 spectral channels, given by the 8 standard BAT bands E1–E8. To determine the spectrum in each channel, the total measured raw photon fluxes in each band were converted into “true” photon fluxes using the calibration determined from the BAT Crab spectrum; we also create a generic redistribution matrix to better represent models with spectral shapes that differ from the Crab (see Section A.1). The uncertainties in each channel were determined from the flux uncertainty for a point source σ_{bgd} (see Section C.1), and then corrected for the effects of source extent as described in Section C.2, Equation (C3), and

Table 3. The final uncertainty is given by σ_{diffuse} in Equation (C3). Additionally, a problem with the implementation of the APEC, which we use as our thermal description for spectral fitting, and MeKaL models in XSpec is that they are undefined above 50 keV. Therefore, for the 4 energy channels above 50 keV, we substitute MeKa for APEC. This should have no significant effect given the small thermal flux at these energies relative to the errors.

For the BAT-only spectra, in which only the nonthermal component of the spatial fit is used to build the spectra, a single power law model is sufficient to measure the nonthermal flux. We also do joint fits of the *Swift* BAT (containing both the thermal and nonthermal spatial components) and *XMM-Newton* spectra. In these fits, the excellent statistics at low energies in the *XMM-Newton* spectra very strongly constrains the thermal emission. However, the *XMM-Newton* mosaic covers a smaller area compared to either the *Swift* BAT or most of the nonthermal spatial models. (The *XMM-Newton* extraction region used for this spectral analysis is indicated by the square in Figure 1.) Thus, in these fits the models applied to the *XMM-Newton* spectra are reduced by the fraction of the emission in our *XMM-Newton* spectral extraction region.

4.1. Joint *XMM-Newton* EPIC-pn – *Swift* BAT Thermal Emission Fit

We first consider a purely thermal model for the X-ray emission in Coma, and fit the *Swift* BAT and *XMM-Newton* spectra simultaneously. The spatial distribution of the emission was assumed to follow the thermal model (Section 3.1.1) as determined from the *XMM-Newton* data. The resulting single temperature fit is presented in Figure 6, and the parameters are given in the first row of Table 1. The quality of the fit is quite good, indicating that a single component description for the temperature structure is sufficient and that the spectra have been reasonably well cross-calibrated. A slight ascending trend in the E1-E3 residuals exists, however, which is primarily due to a slightly lower than expected E1 flux. While not particularly significant, it is worth mentioning several potential causes for the trend. The most straightforward explanation is that the calibration is slightly wrong. We presume the true Crab spectrum to be a simple power law across the entire 2–200 keV interval, but if the spectrum actually steepens around $E \sim 10$ keV as is likely the case (Kirsch et al. 2005), the higher energy bands will be assigned progressively higher flux conversion factors (column 3 in Table 3); basically, the flux in an energy band will be more and more overestimated for bands at higher and higher energies. Also, because emission is more significantly detected in the lower energy bands, a small change in the overall value of the *XMM-Newton* and *Swift* cross-normalization factor – such that the *Swift* flux would be raised – could reduce the spread in residuals. From a more physical perspective, a single temperature model is not

entirely appropriate; in multi-temperature model fits, the trend in residuals is not as strong. In any case, an adjustment to the cross-calibration of 3–5% is sufficient to account for the trend, which is well within our assumed 90% confidence interval uncertainty of 10%.

The best-fit temperature is $kT = 8.24 \pm 0.12$ (stat) ± 0.15 (sys) keV. The systematic term in the error is based on varying the cross-normalization factor by 10%; the origin of this percentage is discussed in Section 5 below. This global temperature matches extremely well with previous measurements. For example, Hughes et al. (1993) found $kT = 8.21$ keV with a spectrum spanning $\sim 2 < E < 11$ keV from the *Ginga* satellite, which had a similar FOV (collimator with 1-2° FWHM) to our aperture, and Arnaud et al. (2001) found $kT = 8.25$ keV over a smaller FOV and lower energy range ($0.3 < E < 10$ keV) with the *XMM-Newton* EPIC-MOS instruments. Including lower energy photons tends to lower single-temperature fits to multi-component spectra (Cavagnolo et al. 2008), and having a smaller FOV tends to emphasize the hotter central temperature of $kT \sim 9$ keV in Coma, which both explains why the *Ginga* and *XMM-Newton* temperatures agree and why the *XMM-Newton-Suzaku* analysis of Wik et al. (2009) found a slightly higher $kT = 8.45$ keV. While we find good agreement with other measurements, note that our temperature, along with other temperatures derived with *XMM-Newton*, could be systematically cooler by a few tenths of a keV than temperatures obtained with other observatories, given the steeper *XMM-Newton* Crab spectrum and the implications for its instrumental response (see Section A.1).

We also tried a two-temperature thermal model for the *XMM-Newton* and BAT data. However, the two temperatures and normalizations could not be individually constrained by the data (Table 1); the temperatures/normalizations listed in the table result when the two-temperature model is fit for with initial temperatures of $kT_1 = 6$ keV and $kT_2 = 10$ keV. The two-temperature fit is not a significant improvement on a single temperature fit.

While the average spectrum in the square degree region around Coma is adequately described with one or two temperatures for the gas, in fact the temperature distribution is quite non-isothermal. We account for temperature variations in the spatial models used to extract fluxes from the BAT images by extrapolating the *XMM-Newton* temperature map from Wik et al. (2009) to higher energies. This map can also be converted into a spectral model (labeled “ T_{map} ” in Table 1) and compared to the joint spectrum. By including the spatial information of the *XMM-Newton* data in the spectral model, we can better account for the thermal contribution in the BAT energy bands. The quality of this fit (allowing the normalization, but not the shape, of the model to vary) is reported in Table 1. In principle, the “ T_{map} ” spectral model should perfectly represent the total *XMM-Newton* spectrum, but due to incomplete coverage of the temperature map with the total *XMM-Newton* region and the imperfect determination of the individual temperatures, the χ^2 value – which is

primarily driven by the higher quality *XMM-Newton* data – is larger than for the other fits, in which the model shape is free to vary and can account for these minor differences. Even so, the BAT data are slightly better described by this model than by any of the other spectral models presented. Although this result is perhaps expected, given that the “ T_{map} ” spatial distribution is used to measure the BAT fluxes, it does indicate that the method is self-consistent.

In all of the thermal models investigated, no evidence for a strong high-temperature component is hinted at by the BAT data.

4.2. Nonthermal Spectra

4.2.1. Nonthermal Emission from the Cluster Center

To search for evidence of more centrally located nonthermal emission, an IC component was first fit to purely thermally-derived spectra – i.e., spectra created from fits to the BAT data using only the thermal spatial model – which are reported in rows 4 and 5 of Table 1. As in Section 4.1, all fits are to the joint *XMM-Newton-Swift* spectrum extracted from the square region in Figure 1. Not surprisingly, the thermal model parameters are almost identical to the fits without the IC component, and no significant IC emission is present. The good single temperature fit to the *Swift* BAT and *XMM-Newton* data already suggests that the nonthermal contribution is not very significant. If the photon spectral index Γ of the nonthermal component is allowed to vary, it is unconstrained and the best-fitted value is unphysically steep, and in any case, only an upper limit can be placed on the nonthermal flux (Table 1). If we assume a photon index of 2.0 for the nonthermal component based on the radio data (Section 5 below), the 90% upper limit on the 20-80 keV flux is 1.24×10^{-12} ergs/s/cm², which corresponds to $< 0.8\%$ of the total flux in the range $2 < E < 200$ keV.

4.2.2. Extended Nonthermal Emission

Our goal is to search for extended nonthermal emission, which is measured with spatial model fits to the unlimited FOV BAT survey images (Section 3.2). Because the thermal and nonthermal spatial model normalizations are individually and simultaneously allowed to vary to best match the total flux in the BAT images, spectra can be created from the sum of both components or separately, and also within any aperture. For each of the 81 grid positions relative to the center of the cluster at which each nonthermal model was fitted for, two spectra are produced. One consists of the total, unvignetted flux of the nonthermal

component only, and the other includes the sum of both the thermal and nonthermal emission inside the *XMM-Newton* extraction region. The second type of spectrum has the advantage that it can be jointly fit with the EPIC-pn spectrum, which in the case of a non-detection provides a tighter constraint on the flux of nonthermal emission than the first type, since the nonthermal component must be consistent with the higher quality, lower energy *XMM-Newton* data as well. In none of these cases, for either type of spectrum, is a nonthermal component detected with $\gtrsim 2\sigma$ confidence. We therefore conclude that, while the *Swift* BAT instrument is certainly sensitive to extended emission, none of a nonthermal origin is observed in the current version of the survey. As an example, the fit parameters for various spectral models are shown in Table 1 for the KW spatial model nominally positioned (i.e. centered on the large-scale *XMM-Newton* emission).

In Figure 7, the nonthermal model with the most significant IC component is shown, assuming a fixed photon index $\Gamma = 2$ for the spectral fits of each nonthermal spatial distribution tried. Note that the model in this figure represents the upper limit for a nonthermal component, not its best-fit value, and that the cross-normalization has been adjusted by 10% in the direction that favors a nonthermal signal. The BAT spectra in Figures 6 and 7 are quite similar, indicating that even in the most favorable case the data reject a significant IC contribution to the spectrum of the Coma cluster, extended or otherwise.

5. Upper Limits to Diffuse, Nonthermal Emission

To ensure appropriate upper limits are derived, we must determine and include any important systematic uncertainties in our results. Typically, instrumental and/or cosmic backgrounds can be a serious concern and must be carefully treated. At lower energies where the thermal emission is bright, the background is not comparable to cluster emission until an energy of ~ 7 keV, so even a background uncertainty of a few percent does not significantly impact the *XMM-Newton* EPIC-pn spectrum. This background includes both the non-X-ray and cosmic backgrounds. Given the size of the mosaic, the uncertainty in the overall EPIC-pn background used here (~ 2 -12 keV) is 2.4% (Read & Ponman 2003). Increasing the *XMM-Newton* background favors larger nonthermal fluxes since this reduces the temperature slightly, so the *XMM-Newton* background is raised by 2.4% during upper limit derivations. Point sources in the *XMM-Newton* mosaic account for only $\sim 1\%$ of the emission and have a spectrum that as a whole does not vary significantly from a $\Gamma \sim 2$ power law (Wik et al. 2009), so we do not model their contribution to the *XMM-Newton* spectrum. While their flux may artificially enhance a nonthermal signal, ignoring them will only result in slightly more conservative upper limits. For the BAT survey data, the

background is automatically removed as part of the image reconstruction procedure, and systematic variations are encoded as fluctuations in empty sky regions, which is already included in the error budget.

The more significant systematic uncertainty is in the determination of the cross-calibration between *Swift* and *XMM-Newton*. Ideally, there should be no uncertainty since we based the BAT calibration on the *XMM-Newton* data and the *Suzaku* XIS0 Crab spectrum. However, the slope of the calibration (i.e. the assumed photon index of the Crab) is less certain. The total error, statistical and systematic, of the photon index in *XMM-Newton* EPIC Crab fits is ± 0.05 (Kirsch et al. 2005), so we adjust our calibration to make the canonical Crab spectrum flatter by 0.05, which acts to increase the BAT fluxes ($\sim 10\%$ for E1, $\sim 20\%$ for E8) and flatten the BAT spectra, thus enhancing nonthermal fluxes. This approach to the systematic uncertainty is also conservative, as it is known that the Crab spectrum steepens above 10 keV (e.g., Kirsch et al. 2005).

Since we have no clear detection of nonthermal emission, we must decide on its photon index from other arguments. The natural choice is to use the spectral index of the radio halo, or $\Gamma = 1.5\text{--}2.5$ (Giovannini et al. 1993), though the lower range of the X-ray regime explored here corresponds to lower energy electrons where the emission may have a flatter spectrum. Also, both previous detections using *RXTE* and *Beppo-SAX* data found $\Gamma \sim 2$, and the model of Kushnir & Waxman (2010) predicts this photon index. Therefore, we fix the nonthermal power law index to $\Gamma = 2$, primarily because we are most interested in directly comparing our upper limits with these previous detections and model predictions. If the spectrum of nonthermal emission is in fact flatter, our upper limits will be low by some amount since the BAT errors are large and the *XMM-Newton* data will have less leverage on the fits. However, the high energy flux will not increase dramatically; as illustrated in Table 3 of Wik et al. (2009), the 20-80 keV flux rises by a factor of 2 from $\Gamma = 2$ to $\Gamma = 1.5$, and trials show the same behavior for the nonthermal component in this work.

For the above systematic uncertainties, we find the 90% confidence upper limits to nonthermal emission for both the nonthermal-only BAT and for the joint EPIC-pn/BAT spectra. The thermal component in the latter case is simultaneously fit with the normalization of the nonthermal component. We present each individual limit in Figure 8 along with the vignetting corrected fluxes/upper limit from *RXTE* (Rephaeli & Gruber 2002, upper cross, green), *Beppo-SAX* (Fusco-Femiano et al. 2004, lower cross, red), and *Suzaku* (Wik et al. 2009, upper limit, blue). The collimator responses for these instruments are convolved with the model flux distributions to give these values or limits. The *Suzaku* HXD-PIN instrument is a square collimator with spatial sensitivity of the form given in Equation 3 of (Wik et al. 2009), and the *RXTE* PCA/HEXTE and *Beppo-SAX* PDS instruments are hexagonal colli-

mators with triangular approximation FWHM of 1° and $1:3$, respectively. We approximate the nearly axisymmetric response with a 4th-order polynomial of the form:

$$R_{\text{hex}}(\theta) = 1.00 - 1.36 \left(\frac{\theta}{\theta_{\text{max}}} \right) + 0.46 \left(\frac{\theta}{\theta_{\text{max}}} \right)^2 - 0.58 \left(\frac{\theta}{\theta_{\text{max}}} \right)^3 + 0.48 \left(\frac{\theta}{\theta_{\text{max}}} \right)^4, \quad (3)$$

where $R_{\text{hex}}(\theta)$ is the fraction of emission visible to the instrument at off-axis angle θ and θ_{max} is where emission is no longer detected. For each spatial model, our upper limits are ordered in Galactic coordinates from the lowest values of l and b in our grid, incrementing l for all positions with that latitude before incrementing b , with l reset to the minimum value. It is this ordering that produces the pattern evident in the limits. The limits for the joint spectral fits are given in the top panel, while the nonthermal-only spectral limits are provided in the bottom panel.

Surprisingly, the upper limits derived from extended spatial models and the BAT data alone (bottom panel) are comparable in sensitivity to the previous detections/limit. Larger models are generally less constrained, due to the greater uncertainty in their estimated flux (Equation C3), though local fluctuations have a greater impact on smaller models, increasing the spread with position. Stronger constraints are obtained when lower energy emission is simultaneously considered (top panel), and a similar range in upper limits is found for each spatial model distribution. This result is not surprising, as each model contributes roughly the same amount of flux inside the *XMM-Newton* extraction region, since most of them are extended beyond this region. Interestingly, the KW model provides the limits most consistent with the *Beppo-SAX* detection, which follows from the large PDS FOV – it would observe a higher proportion of the brighter ring emission – and the larger errors resulting from the KW model’s size. However, in all realizations of the joint fit case, our 90% limits lie below the 90% interval of the previous detections/limit. Thus, all of the previous detections are excluded for any of the spatial models when one fully accounts for the differences in spatial sensitivity between instruments. Our upper limits, for the nominal case where the nonthermal distribution is centered on the large-scale thermal emission, are compared to these previous measurements in Table 2.

6. Implications and Discussion

By taking advantage of the crude imaging capabilities of the *Swift* BAT instrument and the impressive sensitivity of the 58-month all sky survey, we are able to constrain the amount of nonthermal, hard X-ray emission – extended or otherwise – from the Coma cluster. We find no evidence for an extended, hard excess that could reconcile recent detections from *RXTE* (Rephaeli & Gruber 2002) and *Beppo-SAX* (Fusco-Femiano et al. 2004) with the upper limit

from *Suzaku* (Wik et al. 2009); note, however, these detections would still be in conflict with the upper limit of Rossetti & Molendi (2004). Generic, uniform surface brightness disks, along with a recently proposed IC model (Kushnir & Waxman 2010), were fit to BAT survey images, converted to spectra, and investigated for signs of a nonthermal component. For each spatial model, we compute upper limits on a grid of positions and compare them to previous measurements, being careful to convert detected fluxes into intrinsic source fluxes, given a particular spatial distribution, by accounting for the collimator vignetting functions. These are direct comparisons, in the sense that the instrumental response of all detectors involved have been fully considered, and as such we, like Rossetti & Molendi (2004), cannot confirm the claimed detections of Rephaeli & Gruber (2002) and Fusco-Femiano et al. (2004).

Their observed hard excesses could have had other reasonable sources, if not diffuse IC emission from the nonthermal phase of the ICM. A common difficulty is an accurate determination of both the cosmic and non-X-ray background, the treatment of which is the primary difference between Fusco-Femiano et al. (2004) and Rossetti & Molendi (2004). Another possibility is the variable nature of nearby point sources, most notably the AGN W Comae, which was once quite bright but has been fading for many years. The concurrence of the *RXTE* and *Beppo-SAX* observations could have simply been unlucky and caught W Comae (or another source) in a bright state. A somewhat more subtle, and perhaps more likely, explanation concerns the multi-temperature nature of Coma’s ICM. Small amounts of hot gas could dominate the high energy emission, so the extrapolation of an average temperature determined from lower energy data may not be an adequate description of the thermal contribution to the high energy flux. The effect of the multi-temperature gas in Coma is evident in the SW extension at hard energies observed by *INTEGRAL* (Renaud et al. 2006; Eckert et al. 2007) and confirmed here; higher temperatures seen at this location in the temperature map (Wik et al. 2009) are sufficient to explain the change in morphology, which points to the increased significance of this gas at higher energies. Even so, single temperature spectral fits do not produce IC detections in this study or in Wik et al. (2009). A more likely explanation may simply rest in a slight mischaracterization of the hard energy emission weighted temperature; in Fusco-Femiano et al. (2004), the FOV of the lower energy HPGSPC instrument does not quite match the higher energy PDS, and the temperature of 7.67 ± 0.1 keV found in Rephaeli & Gruber (2002) is significantly below that allowed by the *XMM-Newton* data.

Given radio synchrotron emission and an upper limit on the X-ray IC flux, a lower limit on the average ICM magnetic field can be estimated, as described by equation (13) in Wik et al. (2009) and the accompanying text. A diffuse radio flux of 640 mJy at 1.4 GHz is detected out to a radius of $\sim 40'$ in Deiss et al. (1997). For comparison, we will use the upper limit of 2.7×10^{-12} erg s $^{-1}$ cm $^{-2}$ ($20 < E < 80$ keV) from the $R = 40'$ disk model. These values

imply $B > 0.25 \mu\text{G}$, an increase from Wik et al. (2009) but still well below the equipartition value of $B_{\text{eq}} = 0.5 \mu\text{G}$ for the Coma radio halo (Giovannini et al. 1993). A slightly lower limit of $B > 0.2 \mu\text{G}$ results if a more conservative IC upper limit of $4.2 \times 10^{-12} \text{ erg s}^{-1} \text{ cm}^{-2}$ is used, which considers the limits from all spatial models tested. Regardless, these limits on B fall well below line of sight estimates of several μG from Faraday rotation measure (RM) observations (Feretti et al. 1995), though due to geometric effects these measurements may not represent the average cluster magnetic field (Petrosian 2001).

However, the global field may be recovered by combining many RM measurements along different lines-of-sight through the ICM with numerical simulations (Murgia et al. 2004). Bonafede et al. (2010) have applied this method to the Coma cluster, deriving a radial profile where the energy density of the magnetic field falls roughly in proportion with the energy density of thermal gas and with a central field strength of $B_0 \sim 4.7 \mu\text{G}$. Combining this model of $B(r)$ with an approximate representation of the radial density profile of synchrotron emission, implied by a rough β -model fit to the point source subtracted image of Deiss et al. (1997) ($r_c = 18'$, $\beta = 1$, and $I_0 = 1.23 \text{ mJy arcmin}^{-2}$), directly leads to a prediction of the expected IC surface brightness as a function of radius. Our illustrative – due to the large uncertainties in all parameters assumed in this exercise – IC surface brightness distribution is flat out to $\sim 30'$ with a 20–80 keV flux of $\sim 8 \times 10^{-17} \text{ erg s}^{-1} \text{ cm}^{-2} \text{ arcmin}^{-2}$, at which point it nearly linearly drops toward zero, though not reaching it, around a radius of $90'$. This surface brightness is about an order of magnitude below that implied by our upper limits, providing a possible explanation for why we are unable to detect an IC signature. On the other hand, larger IC fluxes would be expected if the radio synchrotron emission falls off more gradually than modeled here, since a flatter radial profile would suggest a higher relativistic electron density given the falling magnetic field with cluster radius. More accurate maps of Coma’s radio halo, preferably at lower frequencies where the radio electrons correspond more closely to the IC-emitting electrons, will clarify this issue.

Ultimately, a true detection of IC emission from Coma will have to wait for upcoming missions with focussing hard X-ray telescopes, namely *NuSTAR*¹ and *Astro-H*². For *NuSTAR* to achieve a sensitivity comparable to our upper limits, a single pointed observation of at least 100 ks will be required (Madsen et al. 2009). However, the much finer spatial resolution will remove the uncertainty associated with bright background AGN and allow multiple spatially-resolved joint fits. Assuming the hottest gas, which produces the largest amount of thermal emission at hard energies, is localized, then these regions can be identified and avoided in

¹<http://www.nustar.caltech.edu/>

²<http://astro-h.isas.jaxa.jp/>

order to detect a lower surface brightness, but more uniform, IC component. Similarly, if the IC emission is more localized, it will be easier to identify with spatially-resolved joint fits between *XMM-Newton* and *NuSTAR* or *Astro-H* spectra, as has been done with *Chandra* data alone (Million & Allen 2009). The unambiguous detection of IC emission associated with radio halos and relics is crucial to determining the energy content in the relativistic phase of the ICM and how significant of an influence this phase has on the dynamics and structure of the thermal gas in clusters.

A. *XMM-Newton* EPIC-pn–*Swift* BAT Cross-Calibration

Because the systematic uncertainties in the survey-averaged spectrum of the Crab Nebula are smaller than the uncertainties in the BAT survey response matrix, BAT survey fluxes are tied to the Crab fluxes in each band since the systematic uncertainties in the survey-averaged spectrum of the Crab Nebula are smaller than the uncertainties in the BAT survey response matrix (see Tueller et al. 2010, Sec. 4.5). This method also requires that the intrinsic Crab spectrum be defined since its exact spectrum remains somewhat uncertain (see Sec. A.2 below), particularly at higher X-ray energies. In practice, though, we are less concerned with an accurate absolute calibration for the BAT than we are with, in this case, an accurate calibration *relative to* our *XMM-Newton* EPIC-pn spectrum. Therefore, instead of prescribing a canonical Crab spectrum as close to the true spectrum as it has been measured thus far, we need to set it to the Crab spectrum as measured by the *XMM-Newton* EPIC-pn instrument *over the energy range we consider*. Otherwise, systematic calibration errors between the instruments could significantly affect our result, since our goal is to detect excess radiation at hard energies due to nonthermal emission. Errors leading to steeper (flatter) *XMM-Newton* spectra and flatter (steeper) *Swift* spectra, for example, will reduce (increase) the thermal contribution at higher energies and similarly enhance (suppress) a nonthermal signal. In other words, any systematic miss-calibrations are mimicked in the BAT calibration so that thermal and nonthermal models can be simply applied during joint fits of the data.

A.1. The Spectrum of the Crab According to *XMM-Newton*

Because of its high X-ray flux, simple spectrum, and lack of significant variability, the pulsar wind nebula of the Crab supernova remnant has been proposed as an X-ray standard flux calibrator (Kirsch et al. 2005). Observations over a large range of energies and with many diverse instruments reveal an intrinsic spectrum nearly consistent with a single power law; however, the photon index and normalization determined by each detector exhibit small

but not insignificant differences (Kirsch et al. 2005; Weisskopf et al. 2010). *XMM-Newton* EPIC-pn measurements, which require that observations are made in burst mode due to *XMM-Newton*'s large collecting area, are best fit with a steeper than average photon index ($\Gamma = 2.13$ versus $\langle\Gamma\rangle = 2.08$ for simultaneous fits to many instrument observations, Kirsch et al. 2005) that is driven by the shape of the spectrum from 0.5-2 keV. However, the residuals to this fit in their Figure 7 suggest that for energies above 2 keV, the *XMM-Newton* photon index is more in line with the average, and since we only consider energies above 2.3 keV, we need to determine what the Crab spectrum is measured to be in this range.

Instead of fitting the Crab spectrum directly, we choose to compare the *XMM-Newton* data to *Suzaku* XIS0 data, which has been well calibrated and consistently fit over its energy range using observations of the Crab. Spectra from each instrument are extracted from identical spatial regions at the center of the Coma cluster (specifically, Region 10 from Wik et al. 2009), where both the gas temperature and surface brightness are roughly constant. Fitting each spectrum from 2.3-12 keV with a single temperature APEC model, we find the *XMM-Newton*-derived temperature to be slightly, though not insignificantly, lower than the *Suzaku* temperature: 8.32 keV versus 8.90 keV. The lower EPIC-pn temperature is consistent with an increasingly larger effective area at higher energies relative to *Suzaku*'s high energy effective area; positing that *XMM-Newton*'s calibration is correct, the relative *Suzaku* effective area at larger energies should be increased as a function of energy, which would lower the flux and therefore the temperature. We model this effect as multiplicative power law component to the *Suzaku* APEC fit, which simultaneously accounts for both the gradient and the overall cross-normalization between the two instruments. Fixing the APEC model parameters to those found with the fit to the *XMM-Newton* spectrum, we find this modification to the *Suzaku* calibration: $f(A_{eff}) = 0.923(E/1 \text{ keV})^{0.045}$. In other words, *Suzaku* spectra are flatter than *XMM-Newton* spectra and have similar hard band fluxes; however, note that the *XMM-Newton* effective area had previously been reduced by 15%, as per the analysis in Wik et al. (2009), in order to match the 2-10 keV EPIC-pn and XIS0 fluxes. Dividing the XIS0 best-fit Crab spectrum of Ishida et al. [$F_{\text{Crab,XIS0}}(E) = 9.51(E/1 \text{ keV})^{-2.05}$, given in *Suzaku* Memo 2007-11³] by $f(A_{eff})$ finally yields the correct parameters for the *XMM-Newton* fit to the Crab spectrum in the energy range of interest:

$$F_{\text{Crab}}(E) = 10.30 \left(\frac{E}{1 \text{ keV}} \right)^{-2.095} \text{ photons/cm}^2/\text{s}. \quad (\text{A1})$$

We take this equation as our canonical Crab spectrum. Then, the true flux of a source in each of the 8 bands is given by the BAT source count rate in that band divided by the observed

³<http://www.astro.isas.ac.jp/suzaku/doc/suzakumemo/suzakumemo-2008-03.pdf>

Crab BAT count rate in that band, and multiplied by the spectrum in Equation (A1) integrated over the band (see Tueller et al. 2010, eqns. 2–4). This conversion factor is reported in Table 3 as the “Flux Calib.”.

While this method is the standard way to create spectra from survey data, it is technically only valid for source spectra that have a shape similar to the Crab. Unfortunately, the survey redistribution matrix, which could properly account for arbitrary spectral shapes, is more uncertain than the observed Crab fluxes (Tueller et al. 2010). Thermal emission above ~ 10 keV is typically much steeper than the spectral index in Equation (A1), so we would prefer to include an approximate redistribution matrix that will handle other such spectral models correctly. To do this, we take a standard response function for an on-axis source from a single observation and multiply the input energies by a smooth function so that the flux-converted Crab spectrum matches Equation (A1) to $< 1\%$ in all energy bands. The addition of this redistribution matrix has a minor effect on spectral fits generally, but it does improve the quality of fits using a thermal model, so we employ it throughout.

A.2. The Hard X-ray Spectrum of the Crab

With this approach, accurate conversions from BAT count rates to true fluxes are not guaranteed. The goal instead is to match the BAT calibration with the EPIC-pn calibration, which ensures that spectral models can be applied seamlessly between the *XMM-Newton* and *Swift* spectra in joint fits. While fluxes quoted hereafter may differ from their true fluxes, the relative amounts of thermal versus nonthermal emission in the joint spectra – considering both their cross-normalization factor *and* shape – are carefully conserved. Ultimately, because our BAT calibration method relies on using the Crab as a flux standard, and since the true Crab spectrum is not known, the choice of a canonical Crab spectrum is at some level arbitrary.

Even so, the hard band fluxes derived herein should be consistent with fluxes derived from other missions. Using the same power law form as for Equation (A1), Kirsch et al. (2005) found a range of normalizations and photon indices for several instruments that overlap with the BAT energy bands: *Beppo-SAX* PDS: $8.84E^{-2.126}$; *RXTE* PCA: $11.02E^{-2.120}$; *RXTE* HEXTE: $9.9E^{-2.090}$; *INTEGRAL* ISGRI: $15.47E^{-2.252}$; and *INTEGRAL* SPI: $15.9E^{-2.203}$. Also, the *Suzaku* PIN fit of $10.93E^{-2.090}$ is consistent with both the scatter in the above results and our adopted spectrum. Ignoring the photon indices derived from *XMM-Newton* data, there seems to be a steepening in the Crab spectrum at higher energies, which means that our relatively flat photon index may over-predict harder band fluxes and thus enhance a potential nonthermal signal. Our Crab spectrum also has a slightly higher overall flux (in

the 20-80 keV band), so that fluxes and upper limits may be biased high, though any such biasing would be well within the absolute calibration uncertainties of all the above missions.

B. Extracting BAT Fluxes from Extended Sources

Very extended, diffuse emission is difficult to detect with coded mask instruments, since the shadow pattern of the mask on the detectors gets smeared out and the signal becomes indiscernible from the background. However, small scale extended emission is detectable, as long as its size is less than the minimum scale necessary to dilute the distinguishability of the mask pattern. In the following, we show that, by simulating extended sources as collections of point sources, this minimum scale is larger than our region of interest and that essentially 100% of the diffuse emission can be detected.

B.1. BAT Point Spread Function

For on-axis sources in the BAT FOV, the point spread function (PSF) has a full width half maximum (FWHM) of $\sim 22'$. Because the sky image is basically the cross-correlation function of the coded mask with the count rates in the individual detectors, it does not represent the intensity per solid angle (i.e. within a pixel). Instead, a pixel value is proportional to the flux of a point source at that location. The width of the PSF is actually due to oversampling the sky plane, not the scattering of photons inside the instrument, and it depends on the size of individual mask element shadows on the detector relative to the size of detector pixels.

As such, the PSF should not be summed in order to derive the source flux – this is provided by the central peak value – and its FWHM depends on the off-axis angle of the source. The distance between the mask and detector increases as the off-axis angle increases, so an angular separation at large off-axis angles produces a more dramatic shift in the shadow pattern across the detector pixels than more on-axis positions, which effectively reduces the oversampling factor and leads to narrower FWHM. Since survey images are created from many “random” individual pointings, each with a given source located at a different off-axis angle, the survey PSF will have an average FWHM and uniform shape, which is roughly Gaussian. Simple Gaussian fits to all the $\gtrsim 10\sigma$ sources in all 8 bands yield an average FWHM of $19'.47$, irrespective of S/N or energy band, essentially identical to the value determined for the 22-month survey (Tueller et al. 2010).

The PSF shape is described by a Gaussian to first order, which is not surprising given

the non-repeating, randomly filled mask and the many pointings that contribute to the flux at each position. However, as is clear from the residuals to a Gaussian fit to the 14–20 keV band Crab data and another source (Cyg X-2) in Figure 9, deviations on the order of 1% of the flux exist (and are significantly larger than the root-mean square (RMS) of the background in this case). While this deviation does not strongly impact the flux of point sources, since only the maximum, central value maps to the flux, a diffuse source is composed of overlapping PSFs, where differences in the wings could affect the overall flux. The residual structure in the wings of the PSF is mainly eliminated by the addition of the two-part function:

$$f(r) = p_0 \left[e^{-r^2/2\sigma_{\text{PSF}}^2} + \frac{1}{120} \begin{cases} \cos x & x < 3\pi \\ -e^{-(x-3\pi)/1.19} & x > 3\pi \end{cases} \right] + p_1, \quad (\text{B1})$$

where r is the distance from the center in arcminutes, p_0 and p_1 are fit parameters (the normalization and background, respectively), $x = 2\pi r/(1.19 \text{ FWHM}) + \pi$, and $\sigma_{\text{PSF}} = \text{FWHM}/(2\sqrt{2\ln 2})$. The improved fit for the Crab is illustrated in the very bottom left panel of Figure 9; while in this case the fit is still not perfect, for other sources the fit is typically better (bottom right panel of Figure 9). We take p_0 to be our measurement of the flux. While the maximum of the PSF may not exactly correspond to p_0 , since all fluxes are determined this way and are also related to the Crab fluxes, any such bias will cancel out during the conversion from BAT count rates to fluxes. Note that the most the additional terms to $f(r)$ could affect a flux, assuming they, for some reason, poorly represented the true PSF shape, is at the $\lesssim 1\%$ level.

B.2. Tests of the Detection of Extended Sources

As discussed in Section 3, we extract fluxes for extended sources by fitting *a priori* model distributions, as opposed to using a method like the “CLEAN” algorithm (Högbom 1974), which reconstructs fluxes from an unknown underlying distribution assuming the PSF shape only. The “CLEAN” method requires some fine-tuning, such as the region of extraction (for clearly detected sources, expanding the region-of-interest even a little beyond the wings of the source can significantly bias the derived flux), “loop gain,” and completion threshold. In our case, since there are only a few likely spatial distributions for the thermal and any potential nonthermal emission, we are less likely to produce biased fluxes by first assuming a spatial distribution than by using a method like “CLEAN.” We represent a diffuse source as a collection of point sources, each of which is convolved by the PSF (Eqn. B1) and summed together.

We now test whether diffuse sources are detectable over our scales of interest can

be evaluated. In general, we treat extended emission as a collection of closely-spaced point sources, since existing software is built with these sources in mind. Point sources at any position in the BAT FOV are straightforward to simulate with the HEASOFT *Swift* task `batmaskwtimg` with the following options set: `coord_type=tanxy`; `distance=1e7`; `corrections=forward,unbalanced,flatfield`; and `rebalance=no`. This task outputs the fraction of each detector pixel which is illuminated by the source at its input position; a value of 0.45 means that 55% of the detector area is shadowed by the mask. At this stage, the detector image can be multiplied by the counts or count rate of the source, and several such detector images representing different sources in the FOV can be added together along with a background – all including Poisson statistics. The background can then be fit and subtracted with the task `batclean`, and finally a reconstructed sky image can be produced via the task `batfftimage`. For now, to isolate the detectability of diffuse emission by the BAT, we simply add uniformly bright, perfectly known point source masks without background or source Poisson noise, to create circular, extended disks of various radii R . Images of the sky are constructed with `batfftimage` for each disk detector image, and the “observed” disk surface brightness profile is fit for as a function of radius. While even large disks ($R \gtrsim 10^\circ$) are visibly noticeable in the sky images, large systematic effects induced by the large spatial extent of the emission lead to large RMS noise that eventually destroys its detectability. The recovered surface brightness, relative to the input level, of simulated diffuse disks of radius R are presented in Figure 10. Error bars represent the simple error of the mean ($\sigma_{\text{RMS}}/\sqrt{N}$, where N is the number of pixels used to determine σ_{RMS}), and the smooth as opposed to random variation around the input surface brightness results from their systematic nature. For sources in the size range of interest to us, $R < 1.5$, the *intrinsic* uncertainty due to the telescope design is $\lesssim 3\%$. As the disk radius increases, the reconstructed surface brightness becomes less and less robust as there are effectively more sources (other parts of the disk) contributing systematic noise to a given location. Note, however, that *all* of the input source flux is recovered.

C. Uncertainties in BAT Fluxes

C.1. Flux Uncertainties for Point Sources

The uncertainty in a given flux measurement is encoded in the RMS fluctuations in the local background (Tueller et al. 2010). These fluctuations represent both the statistical fluctuations from shot noise (dominated by the high background rate) and systematic error contributions from the sky reconstruction process. Due to the large number of individual pointings at nearly random positions, most systematic effects nearly average out and lead to a

symmetric, nearly Gaussian distribution for blank sky regions. We calculate the RMS of the background (σ_{bgd}) around Coma in an annulus of radius $15 < r < 100$ pixels ($42' < r < 4^\circ 67'$), as is typically done for sources in the BAT survey. The values of σ_{bgd} for each band are given in Table 3. While this annulus partially includes the region within which we are searching for a diffuse nonthermal signal, the lack of any obvious emission indicates that the derived errors could not be significantly biased. To ensure σ_{bgd} is not biased by low level extended flux, we recalculated it inside an annulus of equal area with an inner radius of $90'$ and found a nearly identical value of σ_{bgd} in all 8 bands.

C.2. Flux Uncertainties for Extended Sources

The error for a point source, or more correctly the error in the value of a given pixel, presented in Section C.1 does not directly apply to extended sources. Also, we cannot take the standard error from spatial χ^2 fits, using the point source error as the error for the flux in each pixel, because nearby pixels are correlated. Helpfully, the expected error for diffuse sources has already been derived by Renaud et al. (2006) for the IBIS coded mask instrument onboard *INTEGRAL*. In their appendices, they derive source fluxes and errors in reconstructed sky images from detector images and find the straightforward result that the error in a measurement of an extended source flux is proportional to its spatial area normalized by the area of the PSF function (Renaud et al. 2006, Eqn. B3). Specifically,

$$\sigma_{\text{ext}} = \sigma_{\text{bgd}} \sqrt{N_{\text{PSF}}}, \quad (\text{C1})$$

where N_{PSF} is the area of the source normalized by the PSF area. If $I_X(\Omega)$ is the surface brightness of the source convolved with the PSF, I_X^{max} is its maximum value, Ω is the solid angle, and $f(\Omega)$ is the PSF, then

$$N_{\text{PSF}} \equiv \frac{\int I_X(\Omega) d\Omega}{I_X^{\text{max}} \int f(\Omega) d\Omega}. \quad (\text{C2})$$

Before we generally apply Equation (C1) to *Swift* BAT data, we test whether this prescription does in fact apply to extended sources in the *Swift* BAT. For each of the diffuse thermal (Section 3.1.1) or nonthermal (Section 3.1.2) spatial models described above, we created 121 simulations of the extended source and a number of other point sources in the FOV, each with detector counts for the source fluxes and background randomly assigned (taken from a Poisson distribution). Each simulated observation is made from a unique position on an 11×11 grid, with the relative positions of all the sources kept intact. Both the variation of position relative to the telescope axis and the inclusion of point sources are

necessary to fully recreate the systematic contribution to the error. The simulated detector images are then background subtracted and converted into sky images via the procedure outlined in Section B.2. The total flux of the diffuse sources is chosen so that the signal-to-noise ratio is $\sim 20 - 50$. To check Equation (C1), fluxes of all the sources are measured in each simulated sky image, and the average standard deviation of the point source fluxes are compared to the standard deviation of the diffuse source flux. We find that the estimated errors for the diffuse models (Thermal band E1, Disks R25–R60, and KW) generally fall below the expected trend with N_{PSF} in Figure 11. This discrepancy may be due to the number of simulations we were computationally limited to performing – the distribution of fluxes is only roughly Gaussian – or it may represent a true deviation from the results of Renaud et al. (2006). However, to be safe we use Equation (C3) to calculate the error of fluxes extracted with the corresponding model.

There is one additional modification to errors on fluxes extracted with our methodology. Because we fit a spatial model, convolved by the PSF, to the BAT image data, the error in the flux is not just the standard deviation of nearby background pixels, but it depends on how the model is fit to all the pixels. For example, the distribution of normalizations from many fits of a Gaussian function to random data of mean zero and standard deviation σ_{bgd} will not equal σ_{bgd} but some value $< \sigma_{\text{bgd}}$ depending on the pixel scale. A delta function, or Gaussian of width zero, will produce a distribution consistent with σ_{bgd} , since this is identical to measuring the standard deviation, but anything wider finds an average over several pixels, and therefore the distribution of normalizations will tend to be closer to the mean of the random pixels. For our purpose, where the normalization is related to the source flux, the correct error of a flux should come from the distribution of model fits to background, or empty, regions of the survey, which may not be equivalent to σ_{bgd} . Unlike in the above example, neighboring pixels in the survey are correlated due to oversampling – this is essentially the origin of the PSF – and so the standard deviation of model normalizations will be affected by this correlation. Generally, the distribution of normalizations will be larger than σ_{bgd} in this case, as χ^2 minimization will be more influenced by the larger fluctuations near the flux extraction region. The net effect does not significantly change the error distribution shape, but simply inflates the effective standard deviation by some factor, f_m , which is both model-dependent (varying from $1.4\sigma_{\text{bgd}}$ for a point source to $2.24\sigma_{\text{bgd}}$ for the KW model) and energy dependent since the noise properties vary slightly from band-to-band. The total flux uncertainty for a diffuse source in the BAT survey is adjusted from Equation (C1) to become

$$\sigma_{\text{diffuse}} = f_m \sigma_{\text{ext}} = f_m \sigma_{\text{bgd}} \sqrt{N_{\text{PSF}}}. \quad (\text{C3})$$

The precise value of f_m is determined from the standard deviation of fits to 100 blank sky regions, in which we avoid obvious ($> 5\sigma$) sources and the Galactic plane ($b > 20^\circ$). These

factors are reported for each band in Table 3. Not including this error contribution results in spectral fits with unacceptably high χ^2 values.

REFERENCES

- Ajello, M., et al. 2009, *ApJ*, 690, 367
- Arnaud, M., et al. 2001, *A&A*, 365, L67
- Bazzano, A., et al. 1990, *ApJ*, 362, L51
- Briel, U. G., et al. 2001, *A&A*, 365, L60
- Bonafede, A., Feretti, L., Murgia, M., Govoni, F., Giovannini, G., Dallacasa, D., Dolag, K., & Taylor, G. B. 2010, *A&A*, 513, A30
- Cavagnolo, K. W., Donahue, M., Voit, G. M., & Sun, M. 2008, *ApJ*, 682, 821
- Deiss, B. M., Reich, W., Lesch, H., & Wielebinski, R. 1997, *A&A*, 321, 55
- Eckert, D., Neronov, A., Courvoisier, T. J.-L., & Produit, N. 2007, *A&A*, 470, 835
- Eckert, D., Produit, N., Paltani, S., Neronov, A., & Courvoisier, T. J.-L. 2008, *A&A*, 479, 27
- Feretti, L., Dallacasa, D., Giovannini, G., & Tagliani, A. 1995, *A&A*, 302, 680
- Fujita, Y., et al. 2008, *PASJ*, 60, 1133
- Fusco-Femiano, R., dal Fiume, D., Feretti, L., Giovannini, G., Grandi, P., Matt, G., Molendi, S., & Santangelo, A. 1999, *ApJ*, 513, L21
- Fusco-Femiano, R., Orlandini, M., Brunetti, G., Feretti, L., Giovannini, G., Grandi, P., & Setti, G. 2004, *ApJ*, 602, L73
- Fusco-Femiano, R., Landi, R., & Orlandini, M. 2007, *ApJ*, 654, L9
- Giovannini, G., Feretti, L., Venturi, T., Kim, K.-T., & Kronberg, P. P. 1993, *ApJ*, 406, 399
- Harris, D. E., & Romanishin, W. 1974, *ApJ*, 188, 209
- Henriksen, M. J., & Mushotzky, R. F. 1986, *ApJ*, 302, 287
- Högbom, J. A. 1974, *A&AS*, 15, 417

- Hughes, J. P., Butcher, J. A., Stewart, G. C., & Tanaka, Y. 1993, *ApJ*, 404, 611
- Kirsch, M. G., et al. 2005, *Proc. SPIE*, 5898, 22
- Kushnir, D., & Waxman, E. 2010, *Journal of Cosmology and Astro-Particle Physics*, 2, 25
- Lutovinov, A. A., Vikhlinin, A., Churazov, E. M., Revnivtsev, M. G., & Sunyaev, R. A. 2008, *ApJ*, 687, 968
- Madsen, K., Harrison, F., Koglin, J., Mao, P., Craig, W., Pivovarov, M., & Christensen, F. 2009, *Bulletin of the American Astronomical Society*, 41, 347
- Mantz, A., Allen, S. W., Ebeling, H., & Rapetti, D. 2008, *MNRAS*, 387, 1179
- Markwardt, C. B. 2009, *Astronomical Society of the Pacific Conference Series*, 411, 251
- Million, E. T., & Allen, S. W. 2009, *MNRAS*, 399, 1307
- Murgia, M., Govoni, F., Feretti, L., Giovannini, G., Dallacasa, D., Fanti, R., Taylor, G. B., & Dolag, K. 2004, *A&A*, 424, 429
- Nevalainen, J., Oosterbroek, T., Bonamente, M., & Colafrancesco, S. 2004, *ApJ*, 608, 166
- Petrosian, V. 2001, *ApJ*, 557, 560
- Read, A. M., & Ponman, T. J. 2003, *A&A*, 409, 395
- Rephaeli, Y. 1977, *ApJ*, 212, 608
- Renaud, M., Bélanger, G., Paul, J., Lebrun, F., & Terrier, R. 2006, *A&A*, 453, L5
- Renaud, M., Gros, A., Lebrun, F., Terrier, R., Goldwurm, A., Reynolds, S., & Kalemci, E. 2006, *A&A*, 456, 389
- Rephaeli, Y., Ulmer, M., & Gruber, D. 1994, *ApJ*, 429, 554
- Rephaeli, Y., & Gruber, D. 2002, *ApJ*, 579, 587
- Rossetti, M., & Molendi, S. 2004, *A&A*, 414, L41
- Sarazin, C. L. 1988, *Cambridge Astrophysics Series*, Cambridge: Cambridge University Press, 1988
- Schuecker, P., Finoguenov, A., Miniati, F., Böhringer, H., & Briel, U. G. 2004, *A&A*, 426, 387

- Thierbach, M., Klein, U., & Wielebinski, R. 2003, *A&A*, 397, 53
- Tueller, J., et al. 2010, *ApJS*, 186, 378
- Vazza, F., Brunetti, G., & Gheller, C. 2009, *MNRAS*, 395, 1333
- Vanderlinde, K., et al. 2010, arXiv:1003.0003
- Vikhlinin, A., et al. 2009, *ApJ*, 692, 1060
- Weisskopf, M. C., Guainazzi, M., Jahoda, K., Shaposhnikov, N., O’Dell, S. L., Zavlin, V. E., Wilson-Hodge, C., & Elsner, R. F. 2010, *ApJ*, 713, 912
- Wik, D. R., Sarazin, C. L., Finoguenov, A., Matsushita, K., Nakazawa, K., & Clarke, T. E. 2009, *ApJ*, 696, 1700
- Willson, M. A. G. 1970, *MNRAS*, 151, 1

Table 1. Joint Fits to *XMM-Newton* and *Swift* Spectra

Spatial Model	Spectral Model	kT (keV)	Norm. ^a (cm^{-5})	Γ or kT ^b	Norm. ^c	χ^2/dof
Thermal Region	Single T	8.28 ± 0.13	0.373 ± 0.002	-	-	1576.79/1544
Thermal Region	2T ^d	7.8	0.25	9.4	0.12	1575.77/1542
Thermal Region	T _{map}	-	-	-	-	1590.01/1545
Thermal Region	T+IC ^e	8.27 ± 0.13	0.373 ± 0.003	7.2	<0.51	1576.79/1543
Thermal Region	T+IC ^f	8.27 ± 0.13	0.373 ± 0.003	2.0	<0.00148	1577.21/1543
Thermal & KW	Single T	8.30 ± 0.13	0.373 ± 0.002	-	-	1570.32/1544
Thermal & KW	2T ^e	7.8	0.25	9.7	0.12	1568.63/1542
Thermal & KW	T _{map}	-	-	-	-	1584.59/1545
Thermal & KW	T+IC ^e	8.30 ± 0.14	0.372 ± 0.002	-1.5	$<1.9 \times 10^{-9}$	1570.23/1543
Thermal & KW	T+IC ^f	8.30 ± 0.14	0.373 ± 0.003	2.0	<0.00082	1570.62/1543

^aNormalization of the APEC thermal spectrum, which is given by $\{10^{-14}/[4\pi(1+z)^2 D_A^2]\} \int n_e n_H dV$, where z is the redshift, D_A is the angular diameter distance, n_e is the electron density, n_H is the ionized hydrogen density, and V is the volume of the cluster.

^bValue is Γ for the T+IC model and kT (in keV) for the 2T model.

^cValue is the normalization of the power-law component for the T+IC model, which is the photon flux at a photon energy of 1 keV in units of photons $\text{cm}^{-2} \text{s}^{-1} \text{keV}^{-1}$. For the 2T model, the value is the normalization of the second APEC thermal model in units of cm^{-5} .

^dParameters unconstrained.

^eValue of Γ is fixed when deriving errors.

^fValue of Γ fixed based on radio spectrum.

Table 2. Flux Upper Limits (20–80 keV) for Nominal NT Position^a

Model	Joint BAT limit 10^{-12} cgs	<i>Beppo-SAX</i> 10^{-12} cgs	<i>RXTE</i> 10^{-12} cgs	<i>Suzaku</i> 10^{-12} cgs
KW	< 3.86	16.8 ± 5.6	8.3 ± 2.8	< 6.2
R60	< 2.16	19.3 ± 6.4	13.4 ± 4.5	< 25.1
R45	< 2.34	23.0 ± 7.7	18.4 ± 6.1	< 25.4
R40	< 2.53	25.3 ± 8.4	21.0 ± 7.0	< 24.7
R35	< 2.95	26.1 ± 8.7	22.4 ± 7.5	< 21.7
R30	< 3.22	23.7 ± 7.9	21.0 ± 7.0	< 16.8
R25	< 3.48	21.7 ± 7.2	19.7 ± 6.6	< 13.3

^aUnits for flux are 10^{-12} erg cm⁻² s⁻¹

Table 3. *Swift* BAT Error Factors

Band	Energies (keV)	Flux Calib. ^a (cm ⁻²)	$\sigma_{\text{bgd}}^{\text{b}}$	PtSrc f_m	Thermal N_{PSF}	f_m	R25	R30	R35	R40 f_m	R45	R60	KW
E1	14–20	16.55	2.37	1.44	2.09	1.80	1.77	1.60	1.73	1.98	2.08	2.06	2.22
E2	20–24	11.28	1.05	1.32	2.02	1.75	1.39	1.53	1.56	1.22	1.60	1.57	1.94
E3	24–35	10.89	1.63	1.35	1.97	1.59	1.41	1.70	1.82	1.51	1.81	1.91	2.08
E4	35–50	10.46	1.12	1.31	1.90	1.66	1.40	1.59	1.53	1.18	1.62	1.64	2.15
E5	50–75	9.75	1.02	1.30	1.88	1.27	1.59	1.35	1.54	1.28	1.45	1.41	2.04
E6	75–100	13.00	0.99	1.29	2.03	1.34	1.37	1.52	1.25	1.36	1.51	1.57	1.85
E7	100–150	24.48	1.75	1.31	2.67	1.40	1.47	1.59	1.57	1.31	1.52	1.48	1.72
E8	150–195	75.19	3.84	1.31	1.24	1.42	1.45	1.26	1.29	1.23	1.65	1.56	1.93
Diffuse N_{PSF} (indep. of E):				1.00			4.56	6.60	8.98	11.81	14.94	26.42	41.03

^aDefined such that the incidence photon flux at the Earth (photons cm⁻² s⁻¹) is given by the BAT source count rate multiplied by Flux Calib.

^bUnits are 10⁻⁵ cts cm⁻² s⁻¹

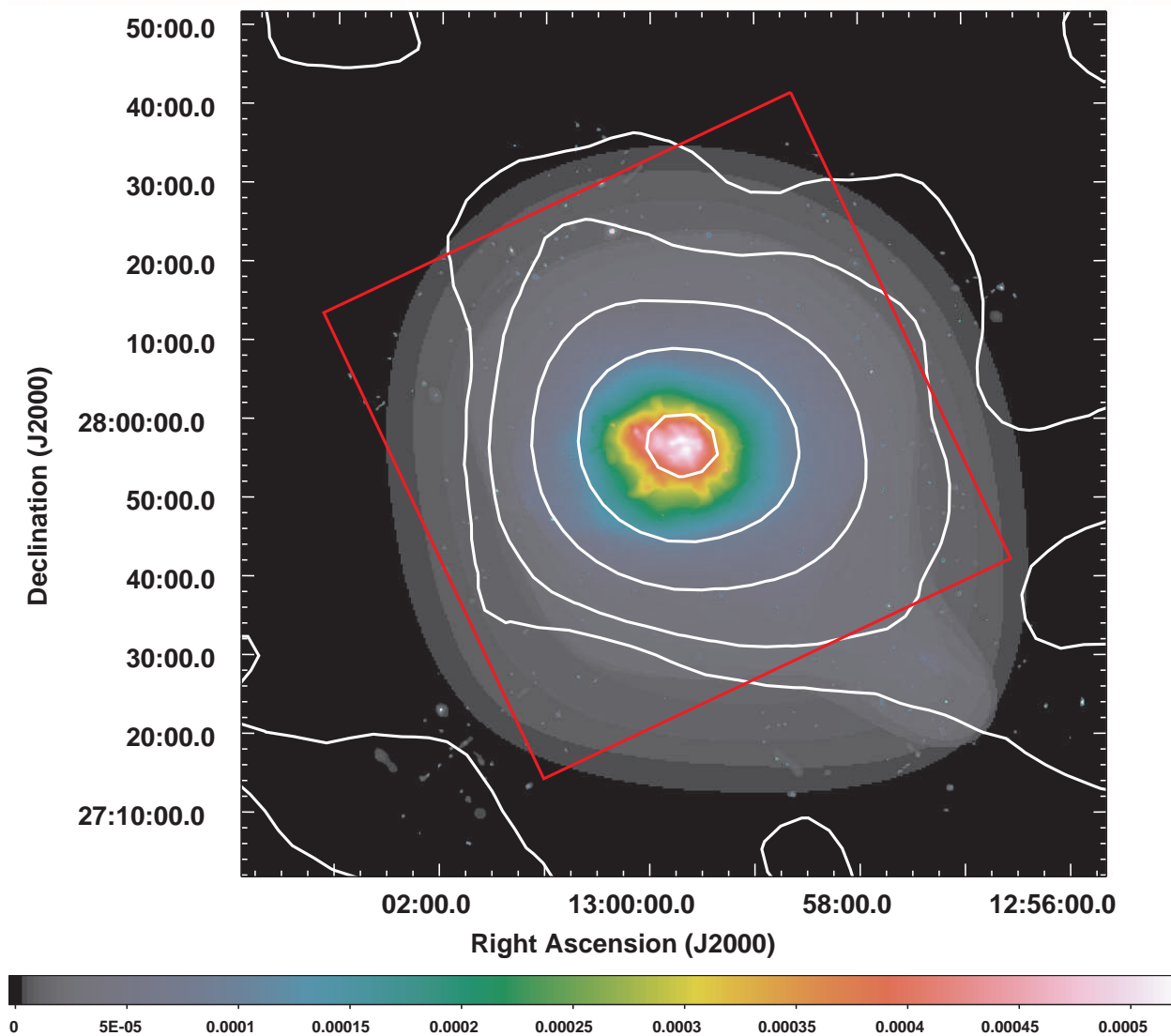


Fig. 1.— *XMM-Newton* EPIC-pn 2–7.5 keV wavelet-smoothed X-ray surface brightness image (Schuecker et al. 2004) with contours from the raw *Swift* BAT 14–20 keV survey image (square root spacing: 0.0, 2.625×10^{-6} , 1.05×10^{-5} , 2.3625×10^{-5} , and 4.2×10^{-5} counts $\text{s}^{-1} \text{pix}^{-1}$). Negative contours are not shown for clarity, and note that the FWHM of the BAT PSF is $19''.5$. The (red) box shows the $65''.5 \times 65''.5$ region from which the EPIC-pn spectrum is extracted for joint fits. The BAT emission is slightly more extended to the W-SW, as would be expected from the higher temperature gas in that direction.

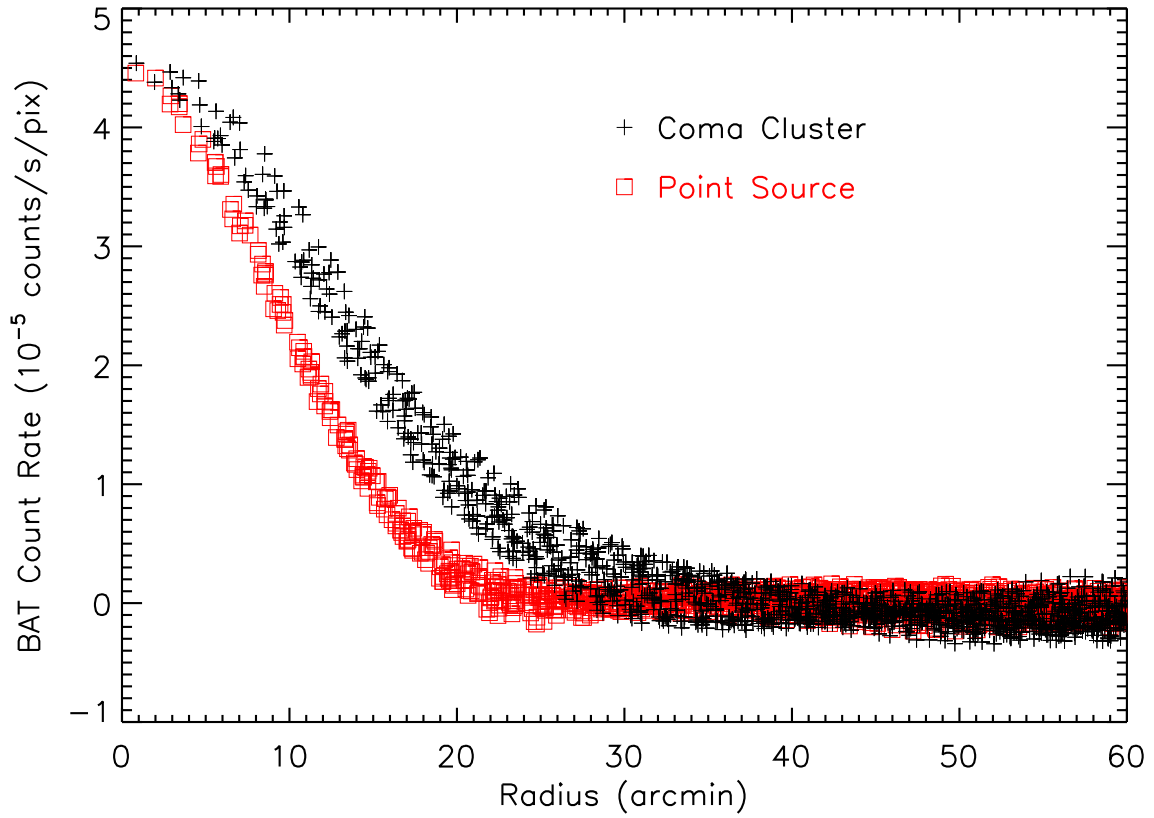


Fig. 2.— The radial profile of the Coma cluster (crosses, black) compared to a point source of comparable brightness (squares, red; scaled slightly to match Coma’s central flux). Each point represents an individual pixel. The BAT emission from Coma is clearly extended and not axially symmetric, as shown by the the larger spread in pixel count rates in its profile compared to the point source.

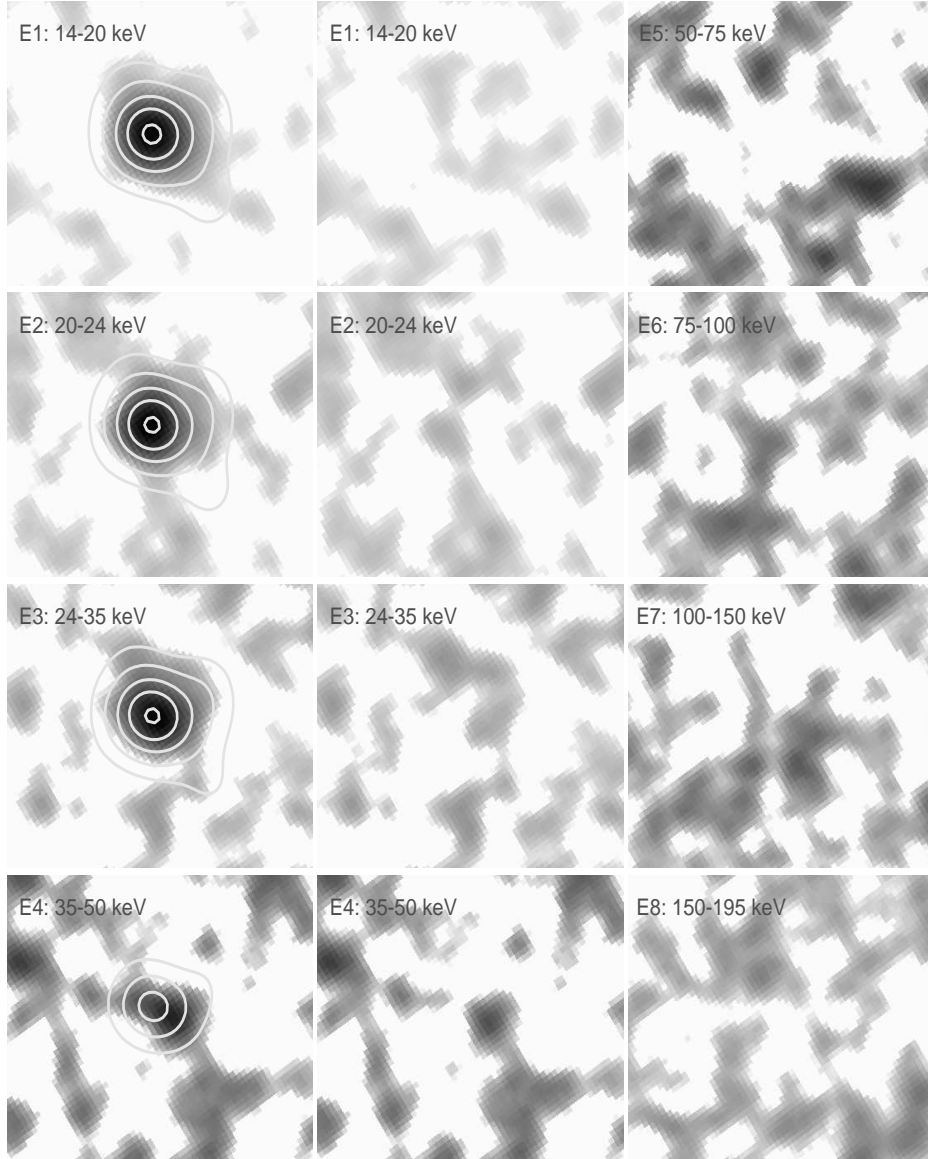


Fig. 3.— Images from the 8 energy bands of the *Swift* BAT survey (first and third columns). The greyscale follows a square root scaling from 0 counts/s (white) to $[> 4.2 \times 10^{-5}$ (E1), $> 1.7 \times 10^{-5}$ (E2–E3), $> 5 \times 10^{-6}$ (E4–E8)] counts $\text{s}^{-1} \text{pix}^{-1}$ (black). The contours in the images in the first column show the best-fit thermal model for each band and follow a square root spacing from 0 to the maximum of the greyscale for that band, with 5 contours. For E4, only three contours are shown as the model is fainter than the brightest region of the data to the west of the cluster center. For E1, the contours occur at the same levels as shown in Fig. 1). The middle column shows the thermal model-subtracted residual images for E1–E4, with the same for greyscale as the data on the left. The residuals show that the thermal spatial models are generally well-mapped to the actual data. Note that the background is also fit for and subtracted from the data in the residual images, so the outer fluctuations are not identical to those in the left column.

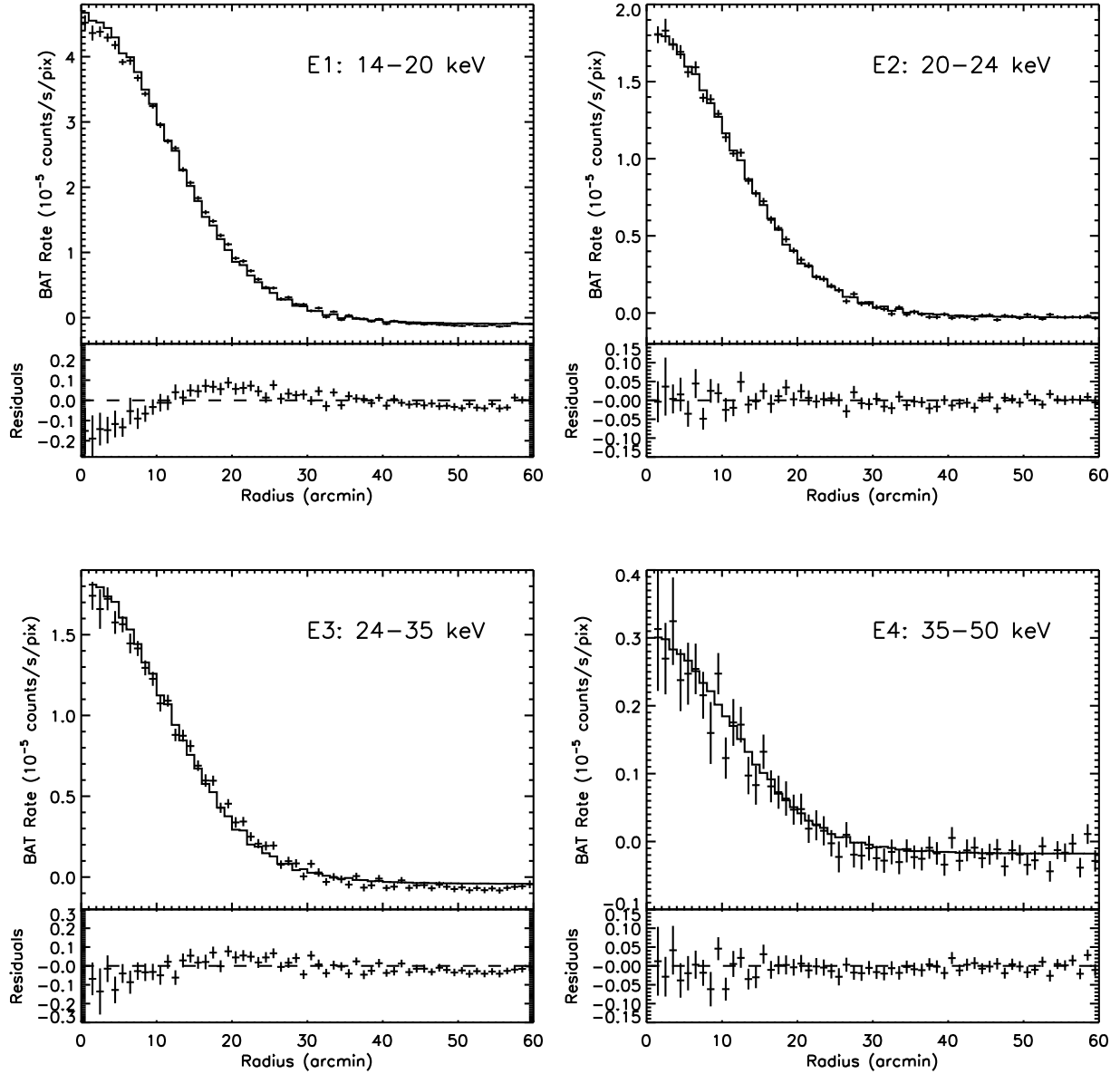


Fig. 4.— Radial profiles of the data and thermal model fits shown in the first column images of Fig. 3. BAT pixels are averaged in annuli of $1'$ width (crosses), as are the model values for each pixel position (histogram); the residuals are plotted below each fit, on the same scale as the fit. The structure in the E1 and E3 residuals could be due to a slightly larger PSF FWHM and/or a true spatial distribution of emission that differs slightly from our models; in either case, the effect on the extracted flux would be less than its 1σ error.

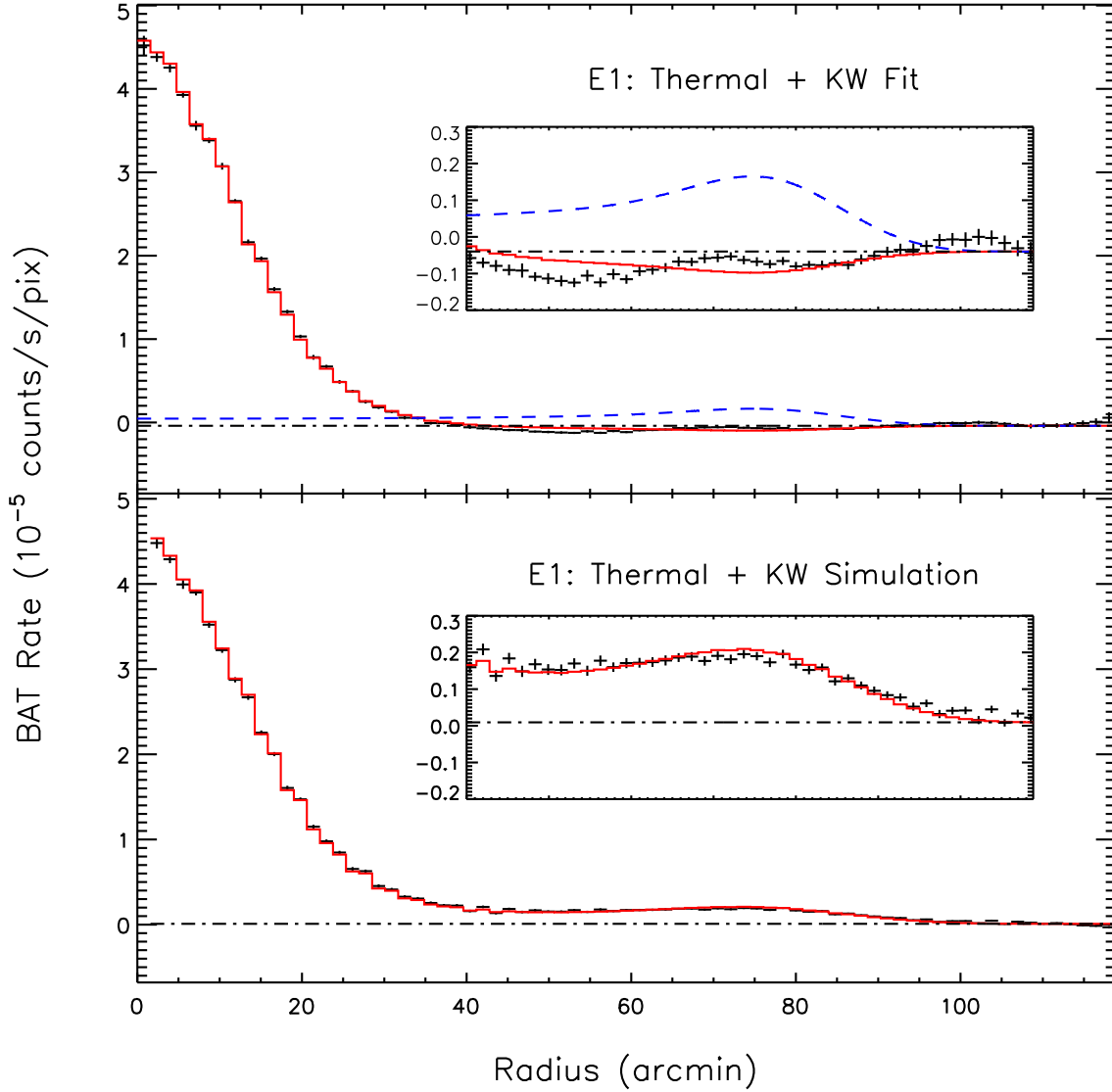


Fig. 5.— The top panel shows the BAT E1 profile and spatial fit for a model with both thermal emission and nonthermal emission following the KW model (histogram, red). The best-fitted value of the normalization of the KW component is actually negative. The dash-dot line represents the background level and the dashed line (blue) shows the predicted spatial distribution of flux for the KW model (Kushnir & Waxman 2010) from 14–20 keV. The inset expands the scale of the y-axis above it to highlight the difference between the data and the expected flux. In the bottom panel, we perform the same fit to simulated BAT data based on the thermal plus KW model, including shot and systematic noise comparable to that present in the actual data. This shows that the BAT would have easily detected a nonthermal component with the spatial distribution given by the KW model and the predicted flux.

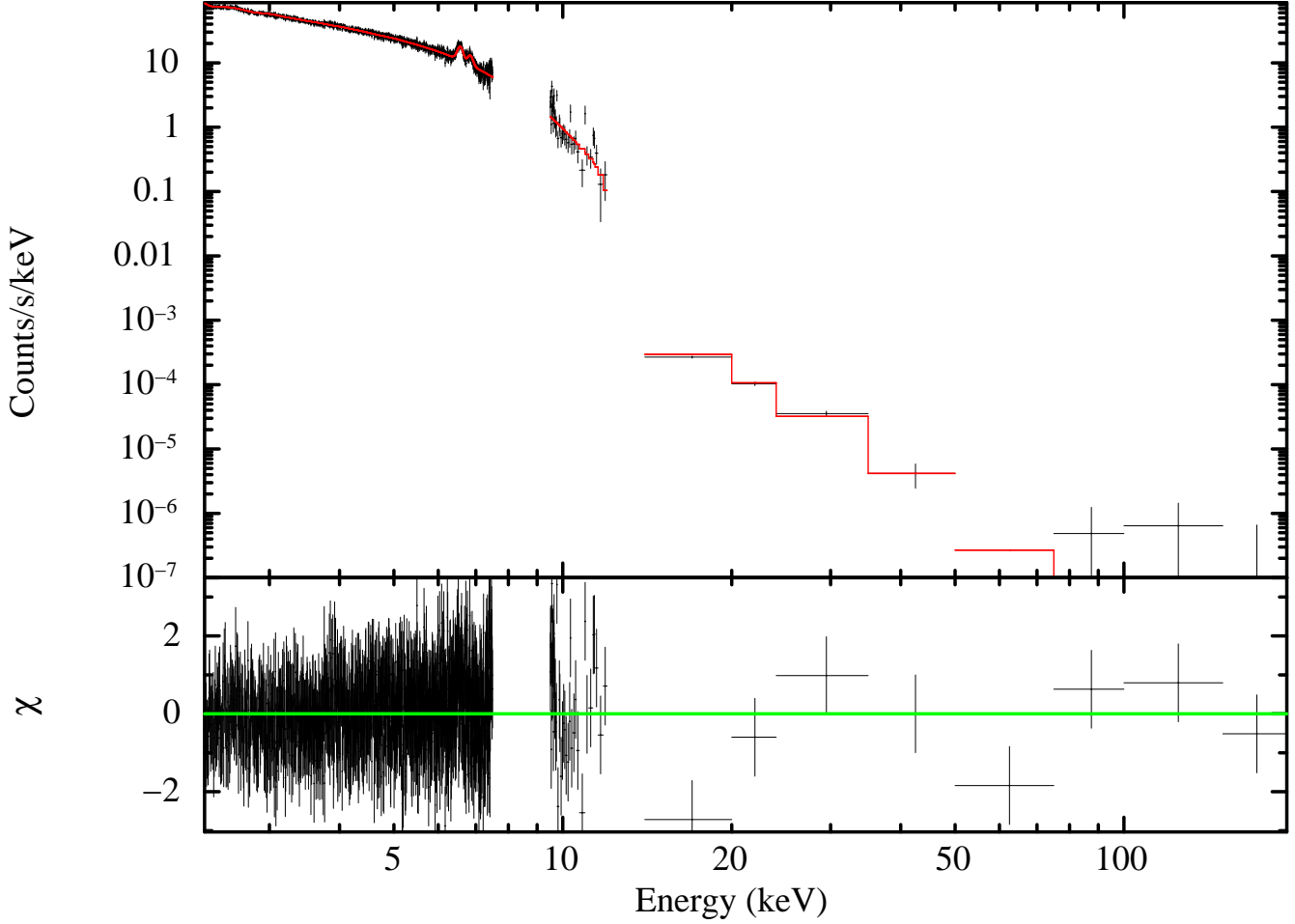


Fig. 6.— Single temperature (APEC) fit to the *XMM-Newton* EPIC-pn and *Swift* BAT spectra. The BAT spectra shown are reduced to the fraction which occurs in the *XMM-Newton* spectral extraction region. The BAT spectra were constructed assuming the spatial distribution predicted by the *XMM-Newton* temperature map. The origin of the low E1 (14–20 keV) flux is discussed in the text. A single temperature model ($kT = 8.24$ keV) is sufficient to describe the 2–200 keV emission from the central square degree region of the Coma cluster.

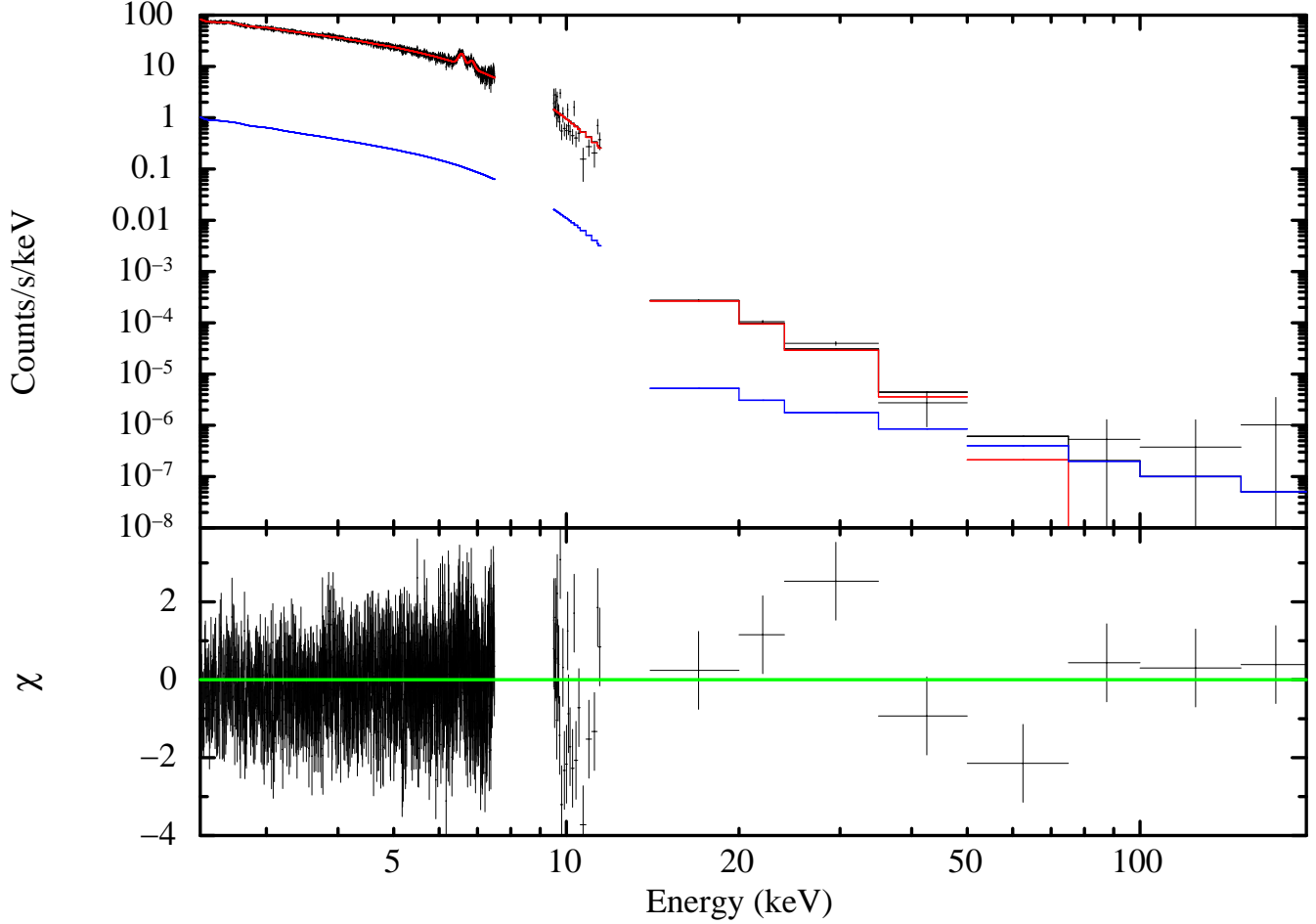


Fig. 7.— Thermal plus nonthermal model fit to the *Swift* and *XMM-Newton* data for the $\Gamma = 2$ power law nonthermal model corresponding to the 90% upper limit, including the systematic uncertainties as described in the text. This example, which is the model with most significant nonthermal flux, is for a $25'$ radius, uniform surface brightness disk of nonthermal emission with a position offset from the center of the large-scale thermal emission by $-2.5'$ and $10'$ in l and b , respectively. As is true of all the upper limits from the joint spectra, the nonthermal component does not exceed $\sim 1\%$ of the low energy part of the *XMM-Newton* spectrum, nor does it compete with the thermal emission until energies $E \gtrsim 50$ keV.

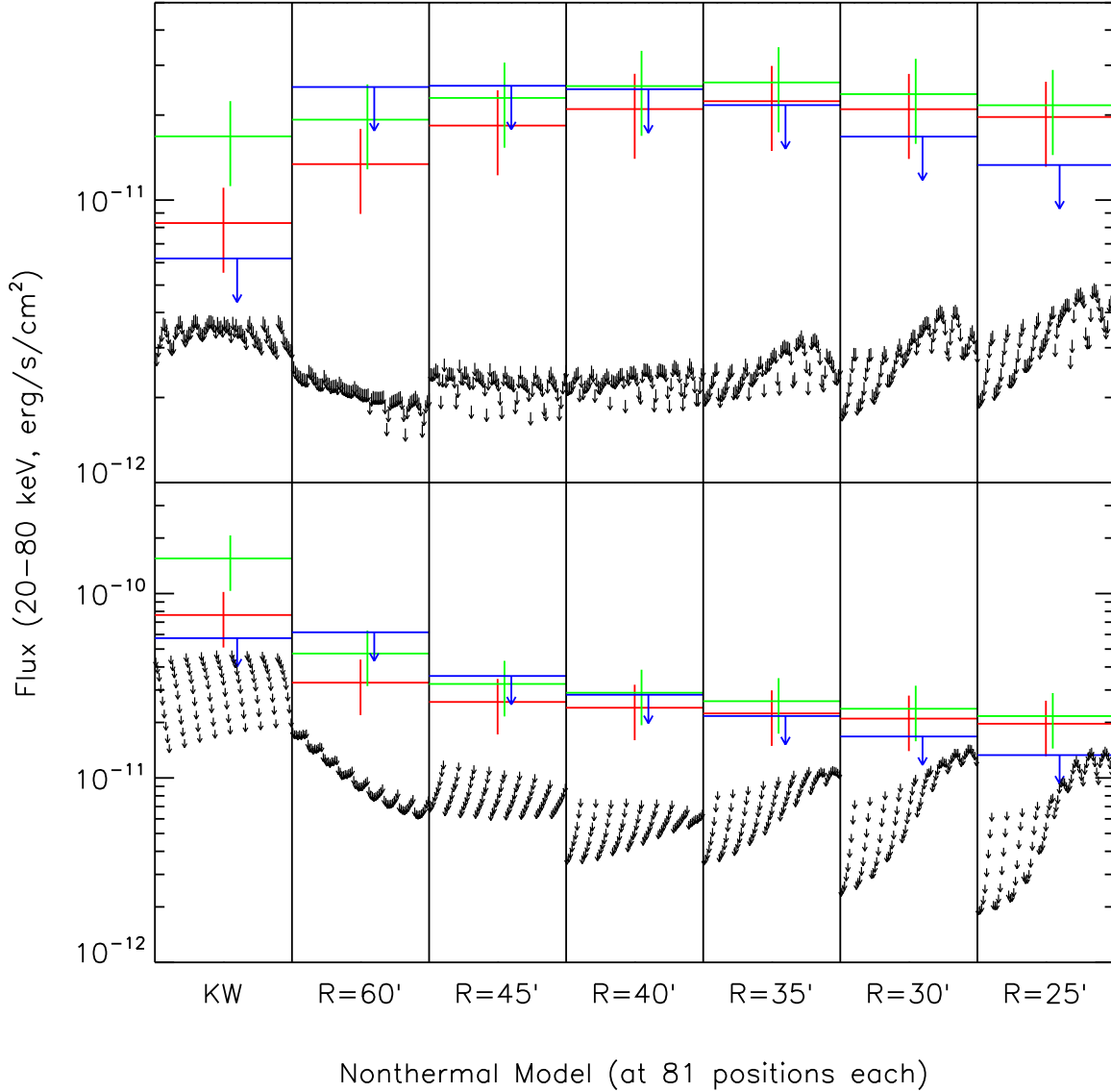


Fig. 8.— Upper limits (small arrows) for each nonthermal spatial model relative to the *RXTE* (Rephaeli & Gruber 2002, upper cross, green), *Beppo-SAX* (Fusco-Femiano et al. 2004, lower cross, red), and *Suzaku* (Wik et al. 2009, long arrow, blue) detections/upper limit. The previous flux detections $[(1.5 \pm 0.5) \times 10^{-11} \text{ ergs/cm}^2/\text{s}]$ and upper limit $(6 \times 10^{-12} \text{ ergs/cm}^2/\text{s})$ are corrected to account for the fraction of emission missed due to vignetting by the collimator response functions (see text). In the top panel, upper limits are calculated from the simultaneous joint fits to the *XMM-Newton* and *Swift* spectra, and all nonthermal fluxes reported are from inside the *XMM-Newton* extraction region (the square in Fig. 1). In the bottom panel, upper limits are derived from BAT spectra created from the nonthermal component of spatial fits *only*, and the fluxes represent the total emission of the spatial model. Based on the results presented in the top panel, we conclude that extended IC emission cannot reconcile the discrepancy between the *Suzaku* and *RXTE/Beppo-SAX* observations.

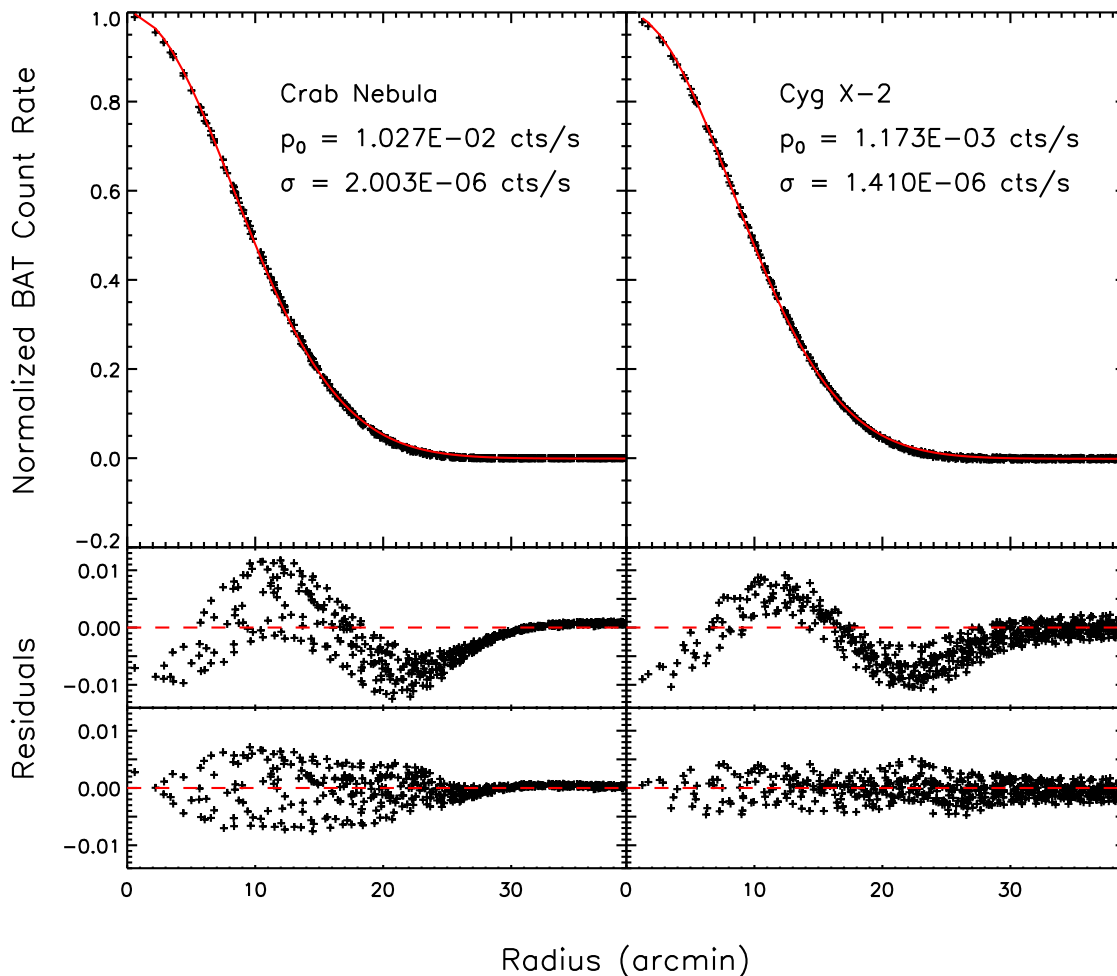


Fig. 9.— Fits to the BAT PSF. In the top and middle panels, the profiles of two point sources, the Crab and Cyg X-2, are fit to a Gaussian. Large, regular residuals (middle panels) remain, which are mostly removed (at the $< 1\%$ level, bottom panels) after modifying our expression for the PSF (Eqn. B1). Lingering residuals, which are particularly significant for the Crab but only slightly noticeable for the other source, primarily result from spatial asymmetries due to the actual angular extent of the source, as in the case of the Crab, and the rectangular shape of the BAT instrument, which will cause off-axis sources to be more “squished” in one direction than another. In the latter case, the effect of summing many individual pointings with the detector in various orientations almost, but not entirely, removes this azimuthal component of the PSF shape.

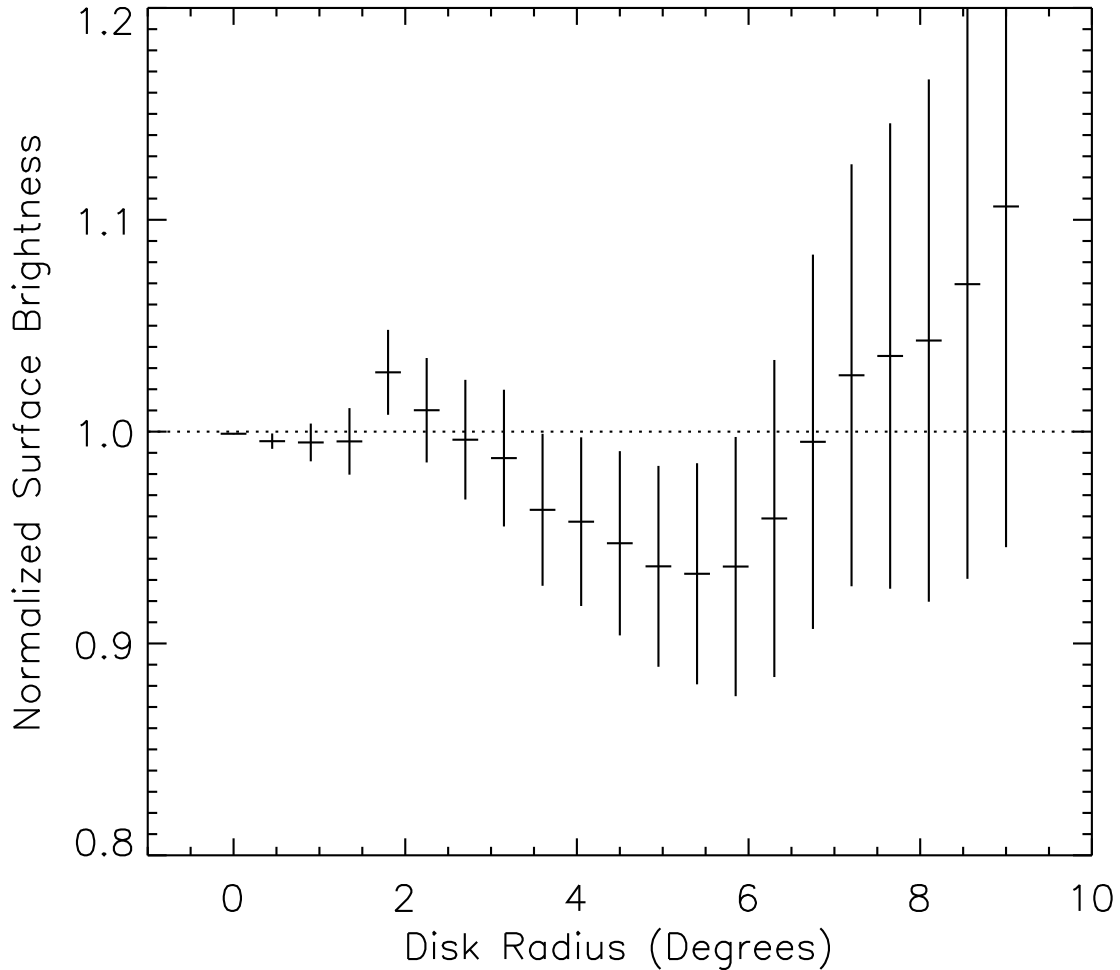


Fig. 10.— Recovered surface brightness for simulated emission from a uniform surface brightness disk of a given radius. Error bars indicate the statistical error of the mean on the disk surface brightness, though the spatial fluctuations in the sky reconstruction behind this error are due entirely to systematic effects; the “noise” at any position in these simulations is determined by the flux of all the other sources within the FOV, or in this case the other parts of the disk. The variation with radius is smooth instead of random due to the systematic origin of the fluctuations. For angular sizes of interest here, $< 90'$, the *intrinsic* uncertainty in the recovered flux of an extended source, due to coded mask imaging techniques, is at most a few percent (based on the size of the error bars). Also, there is *no* loss in sensitivity to diffuse emission; *all* of the input flux is recovered, albeit with less and less precision for larger sources.

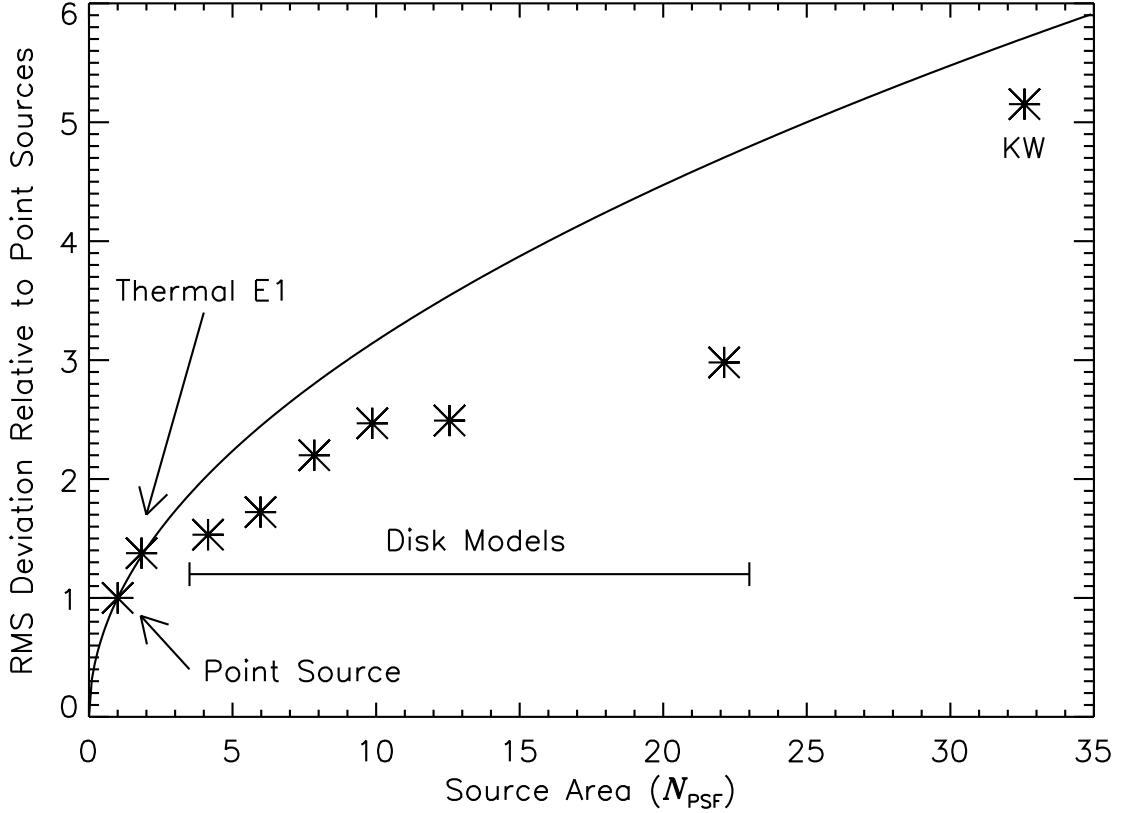


Fig. 11.— The standard deviation of the best-fit normalization for 100 simulations of each spatial model considered in this work. Both photon noise (in the background and source flux) and systematic effects (the influence of other point sources in the FOV and the relative off-axis angle of all sources relative to the detector) are included. The model area is shown in terms of the equivalent number of PSF areas, N_{PSF} . For the thermal spatial models, only the lowest energy band (E1: 14–20 keV) is plotted for clarity. The solid line represents the expected $\sqrt{N_{\text{PSF}}}$ dependence of the error (Equation C1). The simulated values of the errors for the extended models fall below this result, and possible explanations of this behavior are briefly discussed in the text. Note that for the thermal E1 model, the difference in the value of N_{PSF} shown here and in Table 3 results from the difference between the survey PSF and the on-axis PSF used in these simulations.